

# Seismic wave propagation concepts applied to the interpretation of marine controlled-source electromagnetics

Rune Mittet<sup>1</sup>

## ABSTRACT

Concepts such as reflections, refractions, diffractions, and transmissions are very useful for the interpretation of seismic data. Moreover, these concepts play a key role in the design of processing algorithms for seismic data. Currently, however, the same concepts are not widely used for the analysis and interpretation of marine controlled-source electromagnetic (CSEM) data. Connections between seismic and marine CSEM data are established by analytically transforming the diffusive Maxwell equations to wave-domain Maxwell equations. Seismic data and wave-domain electromagnetic data are simulated with 3D finite-difference schemes. The two data types are similar; however, the wave-domain electromagnetic data must be transformed back to the diffusive domain to properly describe realistic field propagation in the earth. We analyzed the inverse transform from the wave domain to the diffusive domain. Concepts like reflections, refractions, diffractions and transmissions were found to be valid also for marine CSEM data but the properties of the inverse transform favored refracted and guided events over reflected and diffracted events. In this sense, marine CSEM data were found to be similar to refraction seismic data.

## INTRODUCTION

Concepts such as reflections, refractions, diffractions, and transmissions are very useful for the interpretation of seismic data. Likewise, these concepts also play a key role in the design of processing algorithms for seismic data. Currently, however, the same concepts are not widely used for the analysis and interpretation of marine controlled-source electromagnetic (CSEM) data. Here, I will dem-

onstrate that these seismic wave propagation concepts can be applied to the interpretation of marine CSEM data. By establishing connections between seismic and marine CSEM data, I hope to make marine CSEM data more accessible to those who have a basic understanding of seismic wave propagation.

Low-frequency electromagnetic fields as we observe them in marine CSEM surveys are diffusive in nature. For the frequency-domain Maxwell equations, we know that the ratio of the imaginary part of the wavenumber to the real part of the wavenumber is of order unity. Lossless and dispersionless field propagation will happen if the imaginary part of the wavenumber is zero and if the phase velocity is independent of frequency. Although this is an approximation that is often used for seismic wave propagation, it is not realistic. Absorption and dispersion effects are present in observed seismic wavefields. Thus, a description of realistic seismic wave propagation requires a complex wavenumber to account for absorption effects and a frequency-dependent phase velocity to give proper causal fields. The frequency dependence of the phase velocity is a consequence of the Kramers-Kronig relation for the real and imaginary part of the wavenumber (Aki and Richards, 1980). Absorption of seismic data is commonly quantified by the dimensionless quality factor  $Q$ . If the absorption effects are not too extreme, we find that the ratio of the imaginary part of the wavenumber to the real part of the wavenumber is approximately  $\frac{1}{2Q}$ . The  $Q$ -factor for sedimentary rocks can be as low as 10 (Newman and Worthington, 1982; Amundsen and Mittet, 1994). More common values are  $Q \sim 30$ – $200$  for sedimentary rocks. An igneous rock such as granite can have  $Q = 1000$ . Thus, we observe that the ratio of the imaginary part of the wavenumber to the real part of the wavenumber is typically two orders of magnitude smaller for seismic wave propagation when we compare with low-frequency electromagnetic field propagation.

Concepts such as reflections and transmissions are used in the analysis of anelastic seismic wave propagation. The reflection and

Manuscript received by the Editor 8 May 2014; revised manuscript received 8 August 2014; published online 4 March 2015.

<sup>1</sup>EMGS ASA, Stiklestadveien, Trondheim, Norway. E-mail: [rm@emgs.com](mailto:rm@emgs.com).

© The Authors. Published by the Society of Exploration Geophysicists. All article content, except where otherwise noted (including republished material), is licensed under a Creative Commons Attribution 4.0 Unported License (CC BY-NC-ND). See <http://creativecommons.org/licenses/by/4.0/> Distribution or reproduction of this work in whole or in part requires full attribution of the original publication, including its digital object identifier (DOI). Commercial reuse and derivatives are not permitted.

transmission coefficients are fully determined by the relevant boundary conditions (White, 1965; Ursin and Stovas, 2002; Carcione, 2007). Carcione (2007) discusses a correspondence principle for seismic waves in which a viscoelastic solution can be obtained if the elastic solution is known. The procedure involves replacing the elastic moduli with the corresponding viscoelastic moduli. This correspondence principle can be applied to the analysis of reflection and transmission coefficients. There is no limitation on the absorption strength when it comes to the validity of this approach. Thus, as an example, if the elastic reflection coefficient is given by the impedances in layer 1 and layer 2 as  $R = (Z_2 - Z_1)/(Z_2 + Z_1)$ , then the corresponding anelastic reflection coefficient will be given as  $R(\omega) = (Z_2(\omega) - Z_1(\omega))/(Z_2(\omega) + Z_1(\omega))$ . The impedances are determined by the elastic or anelastic moduli in layer 1 and layer 2, the corresponding densities and the horizontal wavenumber. As mentioned, the above procedure is valid also for strong absorption. In other words, we do not have to abandon classical concepts such as reflections and transmissions even for strong absorption. However, the frequency-dependent behavior of wavenumbers, reflection coefficients, and transmission coefficients can give rise to very different field behavior depending on whether the absorption effects are weak or strong.

A symmetric treatment of acoustic/elastic field equations and electromagnetic field equations is not new. Auld (1973) discusses the electromagnetic-acoustic analogy in detail and states that a presentation of the acoustic field equations in a form analogous to the Maxwell equations simplifies the task of transferring to acoustics the analytical methodology and techniques that have been applied to solve problems in electromagnetism. The analysis performed by Auld (1973) is valid for conducting media. Ursin (1983) gives a unified treatment of elastic and electromagnetic wave propagation in horizontally layered media. Also, the analysis performed by Ursin (1983) is valid for conducting media and reflection, and transmission coefficients are integral parts of his formalism. The formulation of Ursin (1983) has later been extended to include electromagnetic anisotropy (Løseth and Ursin, 2007). Carcione (2007) devotes one chapter of his book to the acoustic-electromagnetic analogy. He discusses the complete parallelism for the reflection and transmission problem in acoustics and electromagnetism. He considers the most general situation, meaning the presence of anisotropy and attenuation. Attenuation is due to viscosity in the acoustic case and conductivity in the electromagnetic case.

The analysis provided in the present paper is based on a transform method for solving parabolic partial differential equations. The key element of the transform method is that a parabolic partial differential equation can be analytically transformed to a corresponding second-order hyperbolic partial differential equation. The solution of the hyperbolic partial differential equation can then subsequently be back-transformed to give the solution to the proper parabolic partial differential equation. This inverse transform is over the time axis only. Parabolic partial differential equation are typical for diffusion problems, whereas second-order hyperbolic partial differential equation are typical for wave propagation problems. A partial differential equation of the first order in the time derivatives and second order in the spatial derivatives will be parabolic, whereas a partial differential equation of the second order in the time derivatives and second order in the spatial derivatives will be second-order hyperbolic.

Marine CSEM is a low-frequency method. Inspection of the Maxwell equations for a conductive medium shows that there is a

first-order time derivative term giving rise to the conduction current and a second-order time derivative term causing the displacement current. The term in the Maxwell equations giving rise to the displacement current can be neglected for low-frequency field propagation in a conductive medium, such as in marine CSEM. This gives solutions to the Maxwell equations in the quasistatic or diffusive limit that are accurate for marine CSEM applications. Thus, the problem at hand for marine CSEM is the solution of a parabolic partial differential equation. Lee et al. (1989) show that proper solutions to the Maxwell equations in the diffusive limit can be obtained by a transformation method in which the field to be transformed is the solution of a wave equation. A very elegant and useful analysis of this transformation method is given by de Hoop (1996). His formulation of the correspondence principle for time-domain electromagnetic wave and diffusion fields is essential to the discussion that follows.

The present paper demonstrates similarities between seismic wave propagation and field propagation relevant for marine CSEM. The seismic wavefields will be approximated by acoustic fields in this work. The acoustic approximation is sufficient to demonstrate the points I want to make here. The fields in the acoustic and electromagnetic examples will be calculated by 3D finite differences. For the seismic examples, I will use snapshots and shot gathers, and the interpretation of these should be straightforward and familiar. The electromagnetic examples may potentially cause some misunderstanding. The electromagnetic fields shown in the snapshots and shot gathers are in a fictitious time domain. These fields behave like waves and are nondiffusive. However, the transform function that take these fields back to the diffusive, "real world," is known and fairly simple. A key element in this paper is to understand the effect of the transform from the fictitious domain to the diffusive domain. It will be clear from the examples that the electromagnetic fields in the fictitious domain share properties such as reflection, transmission, refraction, and diffraction with the acoustic fields. The question to answer is which of these modes survive the inverse transform from the fictitious time domain to the diffusive frequency domain.

## THEORY

We shall here be concerned with acoustic and electromagnetic field propagation. The underlying simulation method will in both cases be 3D high-order finite differences. The electromagnetic fields will be analyzed in the time and the frequency domain. The following Fourier transform convention is used:

$$\begin{aligned} f(\omega) &= \int_{-\infty}^{\infty} dt f(t) e^{i\omega t}, \\ f(t) &= \frac{1}{2\pi} \int_{-\infty}^{\infty} d\omega f(\omega) e^{-i\omega t}. \end{aligned} \quad (1)$$

Let us first turn to the acoustic case, which is straightforward.

### The acoustic case

The acoustic wave propagation problem is given by Newton's second law and the constitutive relations:

$$\begin{aligned}\nabla \cdot \mathbf{v}(\mathbf{x}, t) + \kappa(\mathbf{x})\partial_t P(\mathbf{x}, t) &= 0, \\ \nabla P(\mathbf{x}, t) + \rho_{ac}(\mathbf{x})\partial_t \mathbf{v}(\mathbf{x}, t) &= \mathbf{f}(\mathbf{x}, t),\end{aligned}\quad (2)$$

where  $\mathbf{v}$  is particle velocity,  $P$  is pressure,  $\mathbf{f}$  is a force-density source function,  $\kappa$  is the compliance or inverse bulk modulus, and  $\rho_{ac}$  is the density. For most of the simulations performed here the density will be kept constant at  $1000 \text{ kg/m}^3$ . The variable density case is discussed in Appendix A. The propagation velocity is given by the compliance and density as

$$c(\mathbf{x}) = \sqrt{\frac{1}{\rho_{ac}\kappa(\mathbf{x})}}. \quad (3)$$

The high-order finite-difference scheme used is an acoustic reduction of the 3D elastic scheme discussed in [Mittet et al. \(1988\)](#). The acoustic field in the simulation examples is excited by a vertical force density. The finite-difference simulations are done for the coupled system in equation 2. The resulting wave equation for the particle velocity is

$$\begin{aligned}\rho_{ac}\kappa(\mathbf{x})\partial_t^2 \mathbf{v}(\mathbf{x}, t) - \nabla \nabla \cdot \mathbf{v}(\mathbf{x}, t) \\ + \nabla \ln(\kappa(\mathbf{x}))\nabla \cdot \mathbf{v}(\mathbf{x}, t) = \kappa(\mathbf{x})\partial_t \mathbf{f}(\mathbf{x}, t),\end{aligned}\quad (4)$$

which demonstrate that the coupled system in equation 2 forms a second-order hyperbolic partial differential equation.

### The electromagnetic case

The electromagnetic part of the present work is based on [Mittet \(2010\)](#), which again is based on [Lee et al. \(1989\)](#) and [de Hoop \(1996\)](#). In particular, [Mittet \(2010\)](#) follows the formulation of [de Hoop \(1996\)](#), the main difference is that [Mittet \(2010\)](#) uses Fourier transforms from time to frequency whereas [de Hoop \(1996\)](#) uses Laplace transforms.

The Maxwell equations in the quasistatic limit are

$$\begin{aligned}-\nabla \times \mathbf{H}(\mathbf{x}, t) + \boldsymbol{\sigma}(\mathbf{x})\mathbf{E}(\mathbf{x}, t) &= -\mathbf{J}(\mathbf{x}, t), \\ \nabla \times \mathbf{E}(\mathbf{x}, t) + \mu\partial_t \mathbf{H}(\mathbf{x}, t) &= 0,\end{aligned}\quad (5)$$

where  $\mathbf{E}$  and  $\mathbf{H}$  are electric and magnetic vector fields. The source term is the electric current density  $\mathbf{J}$ . The conductivity tensor is  $\boldsymbol{\sigma}$ . The finite-difference implementation is anisotropic, but such that only diagonal elements of the conductivity tensor differ from zero. For the following examples of electromagnetic field propagation, it is sufficient to use the isotropic approximation. Thus, the conductivity tensor  $\boldsymbol{\sigma}$  will be replaced with a scalar conductivity  $\sigma$ . The magnetic permeability  $\mu$  is assumed isotropic and equal to the value in vacuum. This is a common assumption for sedimentary rocks. The electromagnetic field in the simulation examples is excited with an electric current density in the  $x$ -direction. The coupled system in equation 5 gives an equation for the electric field as

$$\mu\sigma(\mathbf{x})\partial_t \mathbf{E}(\mathbf{x}, t) + \nabla \times \nabla \times \mathbf{E}(\mathbf{x}, t) = -\mu\partial_t \mathbf{J}(\mathbf{x}, t), \quad (6)$$

which demonstrates that the coupled system in equation 5 forms a parabolic partial differential equation. The frequency-domain representation of equation 6 is

$$\nabla \times \nabla \times \mathbf{E}(\mathbf{x}, \omega) - i\omega\mu\sigma(\mathbf{x})\mathbf{E}(\mathbf{x}, \omega) = i\omega\mu\mathbf{J}(\mathbf{x}, \omega). \quad (7)$$

This system can be solved as a set of linear equations.

The isotropic nondiffusive representation of the Maxwell equations is

$$\begin{aligned}-\nabla \times \mathbf{H}'(\mathbf{x}, t') + \epsilon'(\mathbf{x})\partial_{t'} \mathbf{E}'(\mathbf{x}, t') &= -\mathbf{J}'(\mathbf{x}, t'), \\ \nabla \times \mathbf{E}'(\mathbf{x}, t') + \mu\partial_{t'} \mathbf{H}'(\mathbf{x}, t') &= 0,\end{aligned}\quad (8)$$

where  $\epsilon'(\mathbf{x})$  is the electric permittivity. The primes for the electric fields, the magnetic fields, and the electric permittivity in equation 8 are used to distinguish these fields from the diffusive fields in equation 5. The reason for this is that there is a transformation relation between the nondiffusive field in equation 8 and the diffusive field in equation 5 if

$$\sigma(\mathbf{x}) = 2\omega_0\epsilon'(\mathbf{x}), \quad (9)$$

where  $\omega_0$  is an arbitrary positive constant. The primed fields must be viewed as existing in a fictitious time domain. The transformation relation is discussed in detail in [Mittet \(2010\)](#) in which it is demonstrated that solving the problem in equation 8 with equation 9 gives sufficient information to obtain the field solutions to the diffusive problem in equation 5.

The propagation velocity in equation 8 is given by the magnetic permeability and electric permittivity as

$$c(\mathbf{x}) = \sqrt{\frac{1}{\mu\epsilon'(\mathbf{x})}}. \quad (10)$$

The resulting wave equation for the electric field is

$$\mu\epsilon'(\mathbf{x})\partial_{t'}^2 \mathbf{E}'(\mathbf{x}, t') + \nabla \times \nabla \times \mathbf{E}'(\mathbf{x}, t') = -\mu\partial_{t'} \mathbf{J}'(\mathbf{x}, t'), \quad (11)$$

which demonstrates that the coupled system in equation 8 forms a second-order hyperbolic partial differential equation.

Note that the propagation velocity in equation 10 can be written as

$$c(\mathbf{x}) = \sqrt{\frac{2\omega_0\rho(\mathbf{x})}{\mu}}, \quad (12)$$

with the resistivity  $\rho(\mathbf{x})$  as the reciprocal of conductivity. The resistivity  $\rho(\mathbf{x})$  for the electromagnetic case should not be confused with the constant density  $\rho_{ac}$  for the acoustic case.

From the fictitious time domain to the real frequency domain, the transformation relation between the electric field components is

$$E_i(\mathbf{x}, \omega) = \int_0^T \mathbf{d}t' E'_i(\mathbf{x}, t') e^{-\sqrt{i\omega\omega_0}t'} e^{i\sqrt{i\omega\omega_0}t'}. \quad (13)$$

This is equation 17 in Mitted (2010) and is also the equation I will use here when I analyze the electromagnetic field propagation. The transform in equation 13 is valid with the constraint that  $E'_i(\mathbf{x}, t')$  is causal; hence, we must ensure  $E'_i(\mathbf{x}, t' \leq 0) = 0$ . The fictitious field  $E'_i(\mathbf{x}, t')$  becomes a Green's tensor field  $G'^{EJ}_{ij}(\mathbf{x}, t'|\mathbf{x}_s)$  if it is excited by temporal and spatial Dirac distributions

$$J'_j(\mathbf{x}, t') = \delta(\mathbf{x} - \mathbf{x}_s)\delta(t' - 0^+), \quad (14)$$

where the excitation time is chosen such that the field is causal.

Equations 11 and 17–20 of Mitted (2010) can then be combined to give

$$G'^{EJ}_{ij}(\mathbf{x}, \omega|\mathbf{x}_s) = \sqrt{\frac{-i\omega}{2\omega_0}} \int_0^T dt' G'^{EJ}_{ij}(\mathbf{x}, t'|\mathbf{x}_s) e^{-\sqrt{\omega\omega_0}t'} e^{i\sqrt{\omega\omega_0}t'}. \quad (15)$$

A rigorous derivation of this relation, based on de Hoop (1996), is given in Appendix B.

## RESULTS

Before we can proceed to the simulation examples, I will define events such as *reflection*, *transmission*, *refraction*, *diffraction*, and *guided field* as used in this paper. Some of these terms have different meanings within different fields of physics. The terminology used here is the one most commonly used in the analysis of seismic data. The above-mentioned events are caused by variations in medium properties. For the simplicity of the following discussion, I will assume that these variations in medium properties are velocity contrasts. I will use a half-space model to explain the usage of the above terms by example. I assume that the interface is horizontal and normal to the depth or  $z$ -axis. Sources and receivers are assumed to be in the upper layer. The source is at the origin, and receivers can be at any offset from the source. Furthermore, for this example, I assume that the propagation velocity is higher in the lower layer than in the upper layer. The direct contribution from the source to the receiver is trivial and is not part of the ensuing discussion. Thus, due to the type of velocity contrast, there will be a critical angle as derived by Snell's law. The critical angle can be equated to a critical offset in such a way that for offsets less than the critical offset we have precritical reflections. For angles larger than the critical angle, the absolute value of the reflection coefficient is unity and we observe total reflection of the incoming field. However, there is one additional field contribution present if the lower layer has higher propagation velocity than the upper layer. This additional part of the field enters the lower medium at the critical angle and propagates horizontally along the interface with the velocity of the lower layer. These types of waves are known as *head waves* or *conical waves*. They refract energy back to the upper layer at minus the critical angle. In seismic literature, they are also known as *refracted waves*. At a sufficiently large source-receiver offset, the refracted wave will be the first arrival for the given model. One particular property of the refracted wave is that it will not have the same waveform as the direct wave. As stated in Aki and Richards (1980), the refracted wave will be smoother than the direct wave. The particular type of waveform modification corresponds to an integration in the time domain or a multiplication with  $1/i\omega$  in the frequency domain. The low-frequency part of the spectrum for the refracted wave is

amplified compared with the direct wave. The same waveform modification of refracted events will happen for electromagnetic signals in the fictitious time domain (wave domain). The refraction events will be explicitly identified on snapshots and shot gathers.

For the simulation examples I show here, there is an event that is closely related to the refracted field. It will in the following be denoted as the *guided field*. It will be negligible in the acoustic examples in which a constant density is assumed, but it will be significant in the electromagnetic examples. The acoustic variable density case is discussed in Appendix A. In this case, there are strong guiding effects also for the acoustic case. As stated, the guided field is closely related to the refracted field but is not excited at a single interface. However, if we change the half-space model to a full-space model with a thin horizontal high-velocity layer inside, then guiding may happen. It so happens that for the examples I show here, the constant density acoustic medium will not support a guided field whereas the electromagnetic medium will. Refracted and guided fields will have a linear moveout in a shot gather. The guided field in the wave domain experiences a similar smoothing as the refracted field. It is possible to modify the diffusive domain formalism for the guided field developed by Mitted and Morten (2013) to the wave domain. The result is that the guided response in the fictitious time domain will appear as a smoothed version of the direct signal in the same manner as the refracted signal. The amount of smoothing corresponds to an integration of the direct signal.

The term *transmission* as used here is for field contributions that have a downward propagating component after passing an interface on the way down or an upward propagating component after passing an interface on the way up. Diffractions cannot be explained by the half-space model. They can be caused by different sorts of velocity contrasts. A positive or negative velocity contrast in a full-space model may cause a diffracted event if the contrast has spatial dimensions of the size of a wavelength. As we will see below, diffractions may also be generated by corners or edges in the velocity model. Diffractions will appear as circular or semicircular in the snapshots that follows.

### The seismic case

I will first present results from a seismic/acoustic simulation. It is a deep-water case with generally high propagation velocities in the formation. The results from the simulation of seismic data in this model will be compared with electromagnetic data simulated in an analogous model. A cross section of the velocity model used for the acoustic example is shown in Figure 1. The model is invariant normal to this cross section. The model consists of a 2-km-thick water layer with a propagation velocity of 1500 m/s. The maximum depth of the model is 6 km. The formation propagation velocities are, in general, high. Immediately below the seabed, the propagation velocity is 2683 m/s. On the left side of the model, there is a 1-km-thick layer with a propagation velocity of 5366 m/s. On the right side of the model, there is a 100-m-thick layer with a propagation velocity of 20,782 m/s. This layer starts at a depth of 3.2 km. The lower 2 km of the model consist of a layer with a propagation velocity of 8484 m/s. Propagation velocities in rock are reported up to 8000 m/s. One material that is reported with propagation velocities approaching 20,000 m/s (12,000–18,000 m/s) is diamond. The choice of acoustic propagation velocities will become clear when the electromagnetic example is discussed.

The source is placed at a distance of  $x_s = 0$  km and  $y_s = 0$  km. The source depth is  $z_s = 1.96$  km. Receivers are placed on the seabed from distance  $-9$  km to distance  $9$  km in  $x$  and at  $y = 0$  km. The time behavior of the vertical force density used equals a first-order derivative of a Gaussian with a maximum frequency of  $23$  Hz. The grid step lengths are  $20$  m in all three spatial directions.

Figure 2 shows snapshots of the vertical component of particle velocity. The snapshots in Figure 2a–2d are for times of  $0.45$ ,  $0.69$ ,  $0.93$ , and  $1.66$  s. Figure 2a shows four events. The direct upgoing field is trailed by the seabed reflection. There is a transmitted wave, and there is a strong refracted event due to the large velocity contrast at the seabed. Those four events are also present in Figure 2b. In addition, there is a strong reflection from the thin high-velocity layer on the right side of the model and a modification of the transmitted wave due to the same thin layer.

The most prominent additional events in Figure 2c are two diffractions. One is centered at distance  $-1.8$  km and depth  $3$  km. The second diffraction is centered at the tip of the high-velocity layer. There are also reflections from the bottom layer for this time. Thus, at  $0.93$  s several wave modes are present for this velocity model: direct waves, transmitted waves, reflected waves, refracted waves, and diffracted waves.

The field distribution becomes increasingly complicated at later times as is evident in Figure 2d. The reflection from the free (air-water) surface is a strong event and is also clearly visible. There are also additional refracted events related to the top and bottom interfaces of the left side  $1$ -km-thick layer. Note that these refracted events will be the first arrivals at the seabed receivers at large negative offsets. It is also a buildup of multiple events at later times.

Figure 3 is a shot gather for the acoustic simulation. The recorded data are the vertical component of particle velocity. Some of the events identified on the snapshots are tagged. This will simplify the comparison with the electromagnetic simulation discussed below. Note that the seabed refracted event is the first arrival even at very small offsets and that the moveout is linear.

### The electromagnetic case

We next proceed to the electromagnetic case. A cross section of the resistivity model used for the marine CSEM example is shown in Figure 4. This model has the same geometry as the velocity model in Figure 1. The water layer has a resistivity of  $0.3125$  ohm-m, the top formation has a resistivity of  $1.0$  ohm-m, the  $1$ -km-thick layer on the left side of the model has a resistivity of  $4$  ohm-m, and the bottom layer has a resistivity of  $10.0$  ohm-m. These are all realistic formation

resistivities. The thin layer on the right side of the model has a resistivity of  $60.0$  ohm-m, which is a realistic value for a hydrocarbon-filled reservoir. Note that the resistivity model in Figure 4 is mapped

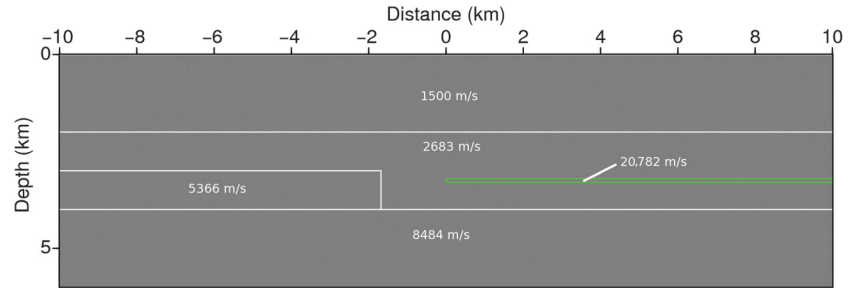


Figure 1. The cross section of the 3D velocity model.

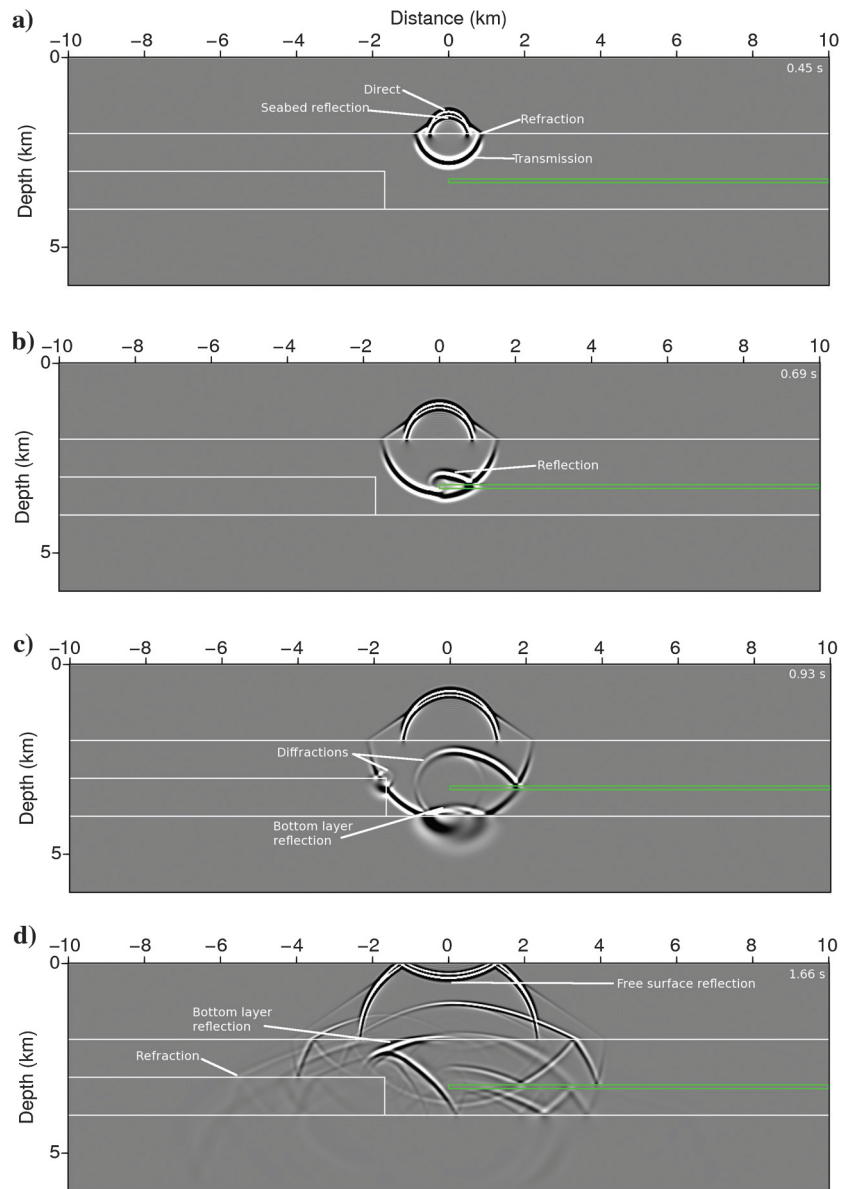


Figure 2. Snapshots of the vertical component of particle velocity.

to the velocity model given in Figure 1 by the resistivity-velocity transformation given in equation 12 if  $\omega_0 = 2\pi f_0$  with  $f_0 = 0.7198$  Hz. The temporal behavior of the transmitter current is identical to the temporal behavior of the vertical force density used as source for the acoustic simulation. Source and receiver locations are identical to those for the acoustic simulations. The source is a horizontal electric dipole oriented in the  $x$ -direction. The grid step lengths are 20 m in all three spatial directions. The high frequency and the fine grid are used here for demonstration purposes. Lower frequencies and a coarser grid are used in practical simulations. These issues are discussed in detail in Mitter (2010).

Figure 5 shows snapshots of the inline component of the electric field  $E_x$ . The electric field is here in the fictitious time domain, thus some care must be taken in the interpretation of these snapshots. However, note that all the information necessary to obtain the proper diffusive electric field is present in the fictitious time-domain field. The snapshots in Figure 5a to 5d are for times 0.45, 0.69, 0.93, and 1.66 s. Figure 5 can be compared to Figure 2. The same events are present in Figure 5a as in Figure 2a. The inline electric field consists of a direct upgoing wave trailed by the seabed reflection. There is a transmitted wave, and there is a strong refracted event due to the large contrast at the seabed.

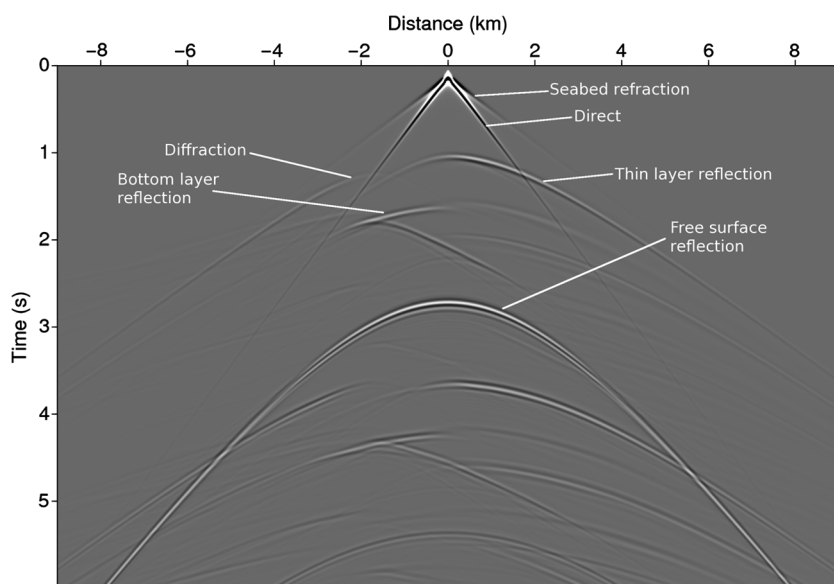


Figure 3. Shot gather for the vertical component of particle velocity.

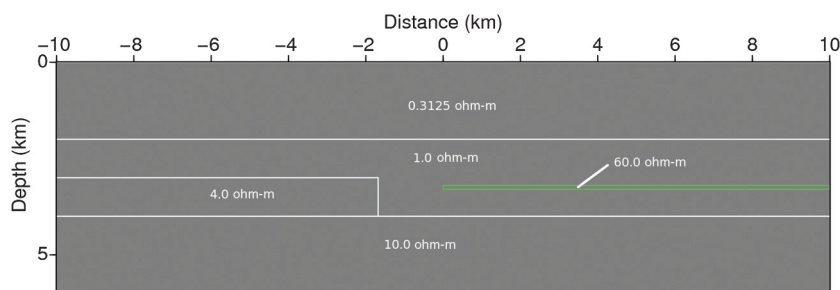


Figure 4. The cross section of the 3D resistivity model.

There is a strong reflection from the thin layer in Figure 5b. This event has a counterpart in Figure 2b. There is an additional event present in Figure 5b with no counterpart in Figure 2b. This is a response from a guided wave propagating as a vertical electric field component in the thin resistive layer. The models used here support a guided wave in the electromagnetic case but not in the acoustic case. The reason for this difference is discussed in Appendix A.

The two diffractions observed in Figure 2c are also present in Figure 5c. The same is the case for the bottom layer reflection. Figure 5d is very close to Figure 2d in terms of number of events and their spatial distribution. Amplitudes will differ for individual events since the governing equations, and hence the reflection and transmission properties differ in acoustics and electromagnetics. However, the similarities between the acoustic and electromagnetic fields are much more striking than their differences. It is undisputed that events such as reflections, transmissions, refractions, and diffractions are present in the acoustic field. Comparing Figure 5 with Figure 2, it is clear that the same is the case for the electromagnetic field as long as it is in the fictitious time domain. However, the transform from the fictitious time domain to the real frequency domain, given in equation 13, is almost trivial and is over the time coordinate only. There is no spatial integration involved in the transform, which implies that any mixing of different events will happen

along the time axis only. This is exactly what happens in a time- to frequency-domain Fourier transform. Consider transforming the acoustic data in Figure 3 from time to frequency. The data have events that can be identified as reflections, refractions, and diffractions. These events must still be considered to be reflections, refractions, and diffractions in the frequency domain. The complex amplitude at a given frequency will contain information from multiple events unless the data are completely dominated by one event only.

Figure 6a shows a snapshot of the inline electric field, and Figure 6b shows a snapshot of the vertical electric field. Both snapshots are at the time of 0.69 s. The scaling is identical for both components. The snapshots demonstrate the fact that the electric field becomes vertically polarized in the thin resistive layer. This vertical component propagates with high velocity in the horizontal direction and inside the thin layer. At the same time, this guided wavefield will couple to the formation above and below and excite horizontal electric field components that travel upward and downward with a propagation direction having a small angle with the vertical axis. This event will be the first arrival at the receivers given a sufficiently large offset. For the given model, the guided event will be the first arrival for offsets above approximately 3 km. The move-out is linear as for refracted waves.

Figure 7 is a shot gather for the electromagnetic simulation. This shot gather shows mostly the same events as the acoustic shot gather in Figure 3. The main difference is the response from the guided wave, which is present in the

electromagnetic data but not in the acoustic data. The shot gather in Figure 3 has one common scale factor for all data points. The same is the case for the shot gather in Figure 7. Thus, many events are hard to identify with this choice of scaling. Figure 8 shows the same data as in Figure 3, but here, each time trace is normalized to unity. There are some undesired effects due to this particular choice of scaling at very large negative and positive offsets, but the result is that many more events become visible. With the chosen scaling, it is easier to expose the properties of the transform from fictitious time to frequency. Figure 9 shows the same data as seen in Figure 7 but with each trace normalized to unity. Comparing Figure 8 and Figure 9, it is striking how similar the acoustic and electromagnetic data are. The main difference is the guided events. The response from the guided wave is marked in Figure 9. Note that approximately 0.5 s later, there follows an event with a similar dip angle. The waveguide is actually triggered more than once for this particular model. The secondary event is triggered by the reflection from the bottom layer. As will be demonstrated below, the transform from fictitious time to real frequency is such that it will weigh down this secondary event relative to the primary event for frequencies above 0.1 Hz, which is in the low-frequency range of marine CSEM survey data.

**From fictitious time to frequency**

The data in Figure 7 are the starting point for the transformation to the diffusive frequency-domain data. The transform kernel in equation 13 has a damping term  $e^{-\sqrt{\omega\omega_0}t'}$  and a phase term  $e^{i\sqrt{\omega\omega_0}t'}$ . Figures 10–15 display the fictitious time-domain electric field multiplied by the damping term for different frequencies. These data sets are damped versions of the data set in Figure 7. Let the damped field be denoted as  $\tilde{E}_i$ , such that

$$\tilde{E}_i(\mathbf{x}, t'|\omega) = E'_i(\mathbf{x}, t')e^{-\sqrt{\omega\omega_0}t'}. \quad (16)$$

The damping term is frequency dependent, and the damping effect increases with increasing frequency.

Figure 10 shows  $\tilde{E}_i$  data for a frequency of 0.01 Hz. There is an amplitude reduction for the late arrivals, but it is a weak effect. The  $\tilde{E}_i$  field must be multiplied by an amplitude-preserving phase term and integrated over time to obtain the frequency-domain electric field. Equation 13 reformulated in terms of the  $\tilde{E}_i$  field is

$$E_i(\mathbf{x}, \omega) = \int_0^T dt' \tilde{E}_i(\mathbf{x}, t'|\omega)e^{i\sqrt{\omega\omega_0}t'}. \quad (17)$$

The above equation behaves as a Fourier transform with an effective angular frequency  $\omega_{\text{eff}}$ , such that  $\omega_{\text{eff}} = \sqrt{\omega\omega_0}$  or effective frequency  $f_{\text{eff}} = \sqrt{f f_0}$ .

At any offset, a multitude of events will contribute to the amplitude and phase of the frequency-

domain electric field. The phase term in equation 17 has the absolute value of unity. For the data shown in Figure 10, we note that early and late arrivals in the fictitious time domain may have a significant contribution to the complex frequency-domain amplitude.

Figure 11 shows  $\tilde{E}_i$  data for a frequency of 0.033 Hz. Comparing Figure 11 to Figure 10, the effect of the transform for increased frequency becomes clear. The late arrivals have a reduced amplitude. This makes perfect sense because the frequency-domain field in equation 17 is diffusive in nature and the skin depth effect must apply to this field. The skin depth effect dictates that as the frequency increases the field contributions that have a long propagation path should be reduced in amplitude. The damping effect can be seen to increase further from Figure 12 to Figure 15 in which the frequency increases from 0.1 to 3.33 Hz.

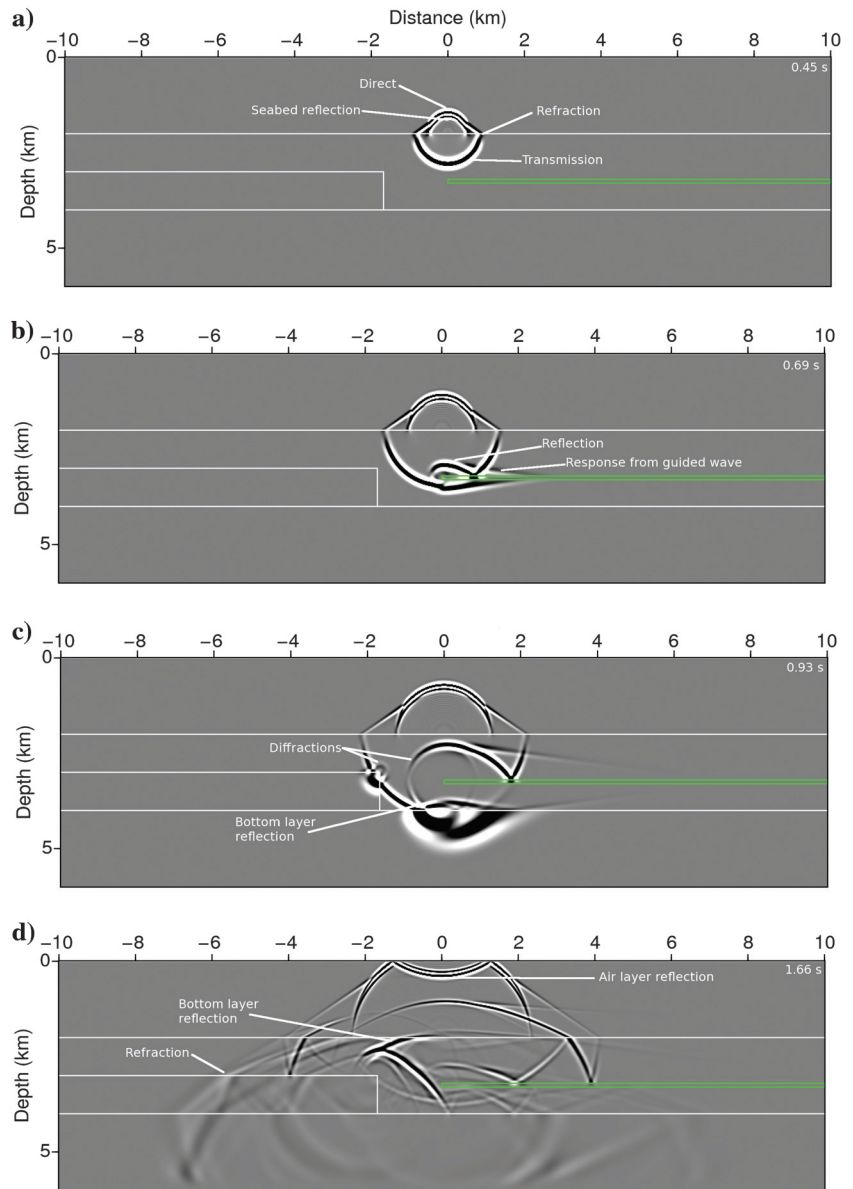


Figure 5. Snapshots of the inline electric field.

The damping effect is the dominating effect when the frequency-domain electric field is extracted from the fictitious time-domain electric field and the frequency is 0.1 Hz or higher. However, there is an additional, more subtle effect that must be considered for frequencies below 1.0 Hz. Let us take the 0.333 Hz data in Figure 13 as an example. The time traces at offsets  $-6$  km and  $+6$  km are shown strongly amplified. For the trace at  $+6$  km, there are four remaining events after the application of the damping term. The first arrival at 1.25 s is the guided event. The second arrival at 1.75 s is also a guided event, but excited by the upcoming reflected field. The third event at 2.3 s, which is fairly weak, is the field refracted below the seabed. The fourth event at 2.45 s is strong. This is the reflection from the thin high-resistivity layer. Apparently, this event should

contribute significantly to the transform from the fictitious time domain to the frequency domain. The conclusion would then be that it is the reflection that gives the main contribution to marine CSEM data at large offsets and not the response from the guided wave. This is not so. This can be verified by inspecting the cumulative behavior of the frequency-domain response in equation 17:

$$E_i(\mathbf{x}, \omega) = \int_0^{\tau} dt' \tilde{E}_i(\mathbf{x}, t'|\omega) e^{i\omega_{\text{eff}} t'} + \int_{\tau}^T dt' \tilde{E}_i(\mathbf{x}, t'|\omega) e^{i\omega_{\text{eff}} t'}. \quad (18)$$

The second term on the right side has only negligible contributions to  $E_i(\mathbf{x}, \omega)$  if the split in time integration is set to  $\tau = 2$  s. Thus, the integration over the refracted event and the reflected event that arrives later than 2 s does not contribute significantly to the complex amplitude. In fact, the transformation over the two first, guided events gives 95% of the contribution to the amplitude of the frequency-domain response. The refracted event is small in the fictitious time domain, so a small contribution to the frequency-domain amplitude can be expected. However, the relatively large reflected event gives only a small frequency-domain contribution. This requires an explanation.

First, it is important to note that the effective frequency in the Fourier transform in equation 17 is small compared with the dominant frequency for the signals in the fictitious time domain. The effective transform frequency in equation 17 is  $f_{\text{eff}} = 0.49$  Hz. The dominant frequency for the signals in the fictitious time domain is 10 Hz, and the maximum frequency is greater than 20 Hz. The Fourier transform in equation 17 will depend on the low-frequency part of the spectrum of the signal in the fictitious time domain. It has already been mentioned that the refracted and guided responses in the fictitious time domain will be smoother than the direct and reflected contributions and that this smoothing effect amounts to a time integration of the emitted signal from the transmitter. In these simulations, the transmitter current varies as the first-order derivative of a Gaussian. The direct electric field below a horizontal electric dipole will dominantly have a signal form that goes as the time derivative of the current (see equation A-5 in Mittet, 2010). That is the second-order derivative of a Gaussian (Ricker wavelet) for the given example. There are also near-field contributions that behave as the first-order derivative of the Gaussian or the Gaussian itself, but these contributions can be neglected at distances above a few typical wavelengths or for distances above approximately 300 m for the examples here. The reflected waveforms will also be proportional to the second-order derivative of a Gaussian. However, refracted and guided events will be proportional

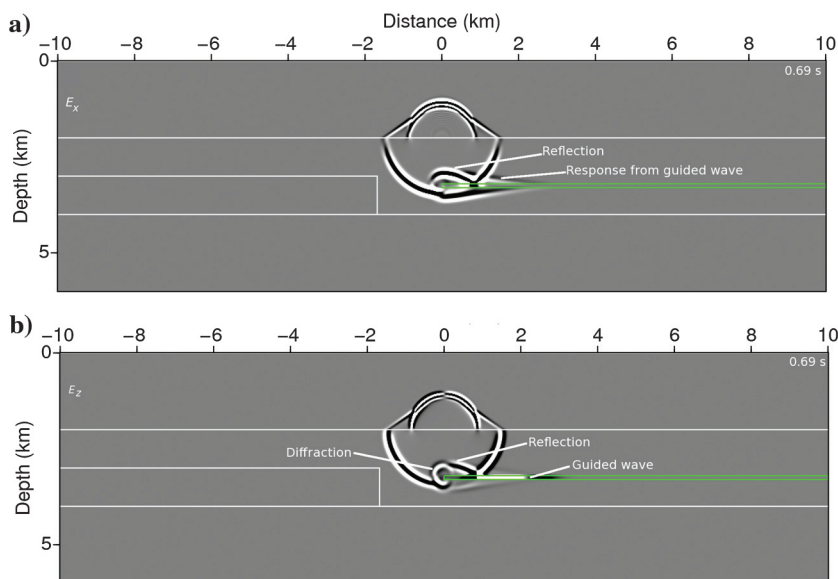


Figure 6. (a) Snapshots of the inline and (b) the vertical electric fields.

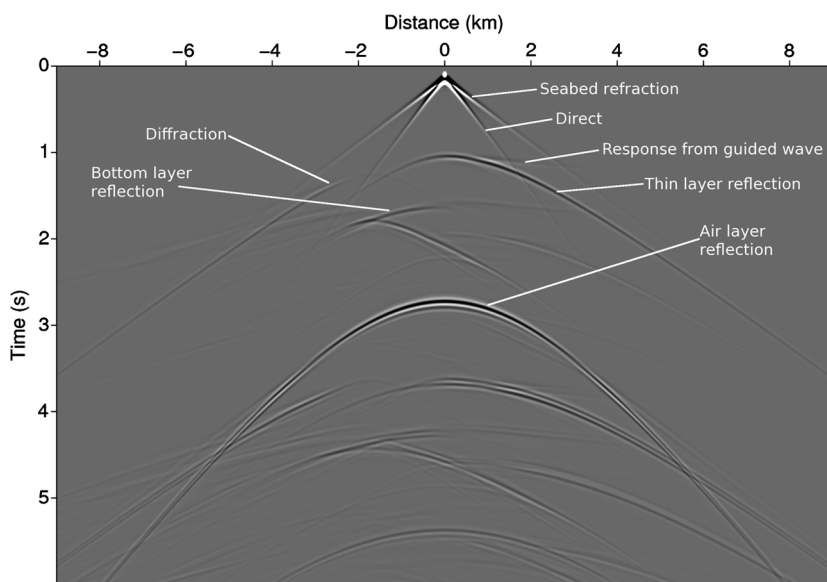


Figure 7. Shot gather for the inline electric field.



to the first-order derivative of a Gaussian. In Appendix C, I demonstrate how the first- and second-order derivatives of the Gaussian contribute to the transform in equation 13 or the equivalent transform in equation 17. A result from Appendix C is that a time-domain signal proportional to the second-order derivative of the Gaussian may have a much larger amplitude than a time-domain signal proportional to the first-order derivative of the Gaussian and still give a much smaller frequency-domain contribution in the transform defined by equation 17. Gaussian waveforms are convenient for the examples, but these results are valid for other transient and band-limited waveforms. The smoothing effect experienced by refractions and guided events will boost the low-frequency components of the signal spectra compared with direct and reflected events. The effective transform frequency in equation 17 is small and will be sensitive to these modifications of the low-frequency components of the signal spectra. Thus, the net effect for the trans-

form from the fictitious time domain to the frequency domain is that refracted and guided events will give relatively larger contributions to the complex field amplitude than reflected events.

This effect is apparent for the first event on the +6 km trace in Figure 13. The guided response behaves as a first-order derivative of a Gaussian prior to the application of the damping term. The integral over the guided event at 1.25 s gives the main contribution to the complex frequency-domain amplitude. The rest of the contribution comes from the additional integral over the second guided event at 1.75 s.

Refracted events are smoothed in the same way as the guided events. The net effect is that also these types of events give relatively large contributions when the electromagnetic fields are transformed from the fictitious time domain to the diffusive frequency domain. The contribution from the refracted event at time 2.3 s and offset +6 km in Figure 13 is small because the amplitude is relatively

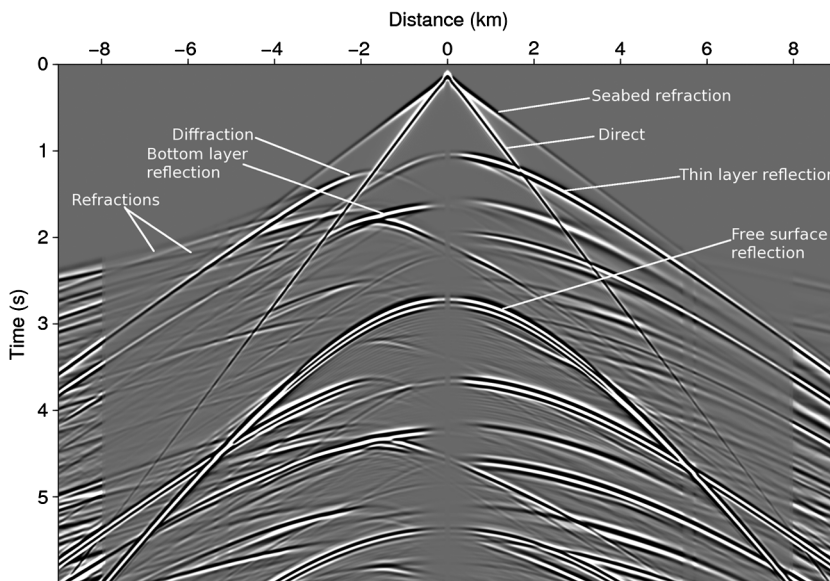


Figure 8. Normalized shot gather for the vertical component of particle velocity.

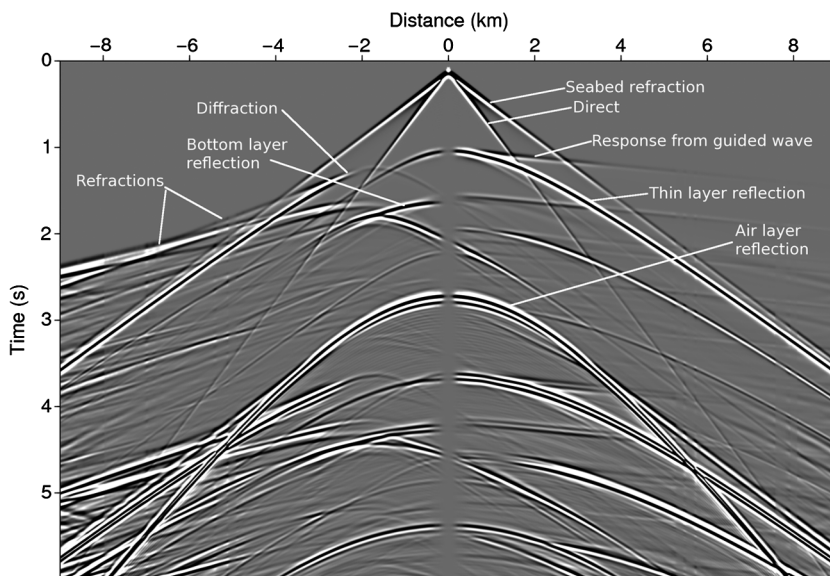


Figure 9. Normalized shot gather for the inline electric field.

small. However, this event is important at smaller offsets. From Figure 13, we see that it is stronger than the guided event up to 3 km. The refracted event would give the main contribution to the observed field also at large offsets in the absence of the thin resistive layer. The 1-Hz data are shown in Figure 14. The damping effect is now so strong that the guided event at 1.25 s completely dominates. Figure 15 shows the damped electric field at 3.33 Hz. The only surviving contribution is the guided field.

For frequencies between 0.1 and 3.33 Hz, which are in the typical marine CSEM frequency band, we observe that at any offset the early arrivals give important contributions to the frequency-domain data. Early arrivals at intermediate and large offsets are usually refracted and guided events. Reflections and diffractions at intermediate and large offsets are late arrivals. Their contribution is less important in marine CSEM compared with refracted and guided

events. This effect is exposed by analyzing the marine CSEM experiment in the fictitious time domain in which contributions from late-arriving reflections are quenched by the exponential damping term in the transform. As mentioned, there is an additional effect in the transform from fictitious time to diffusive frequency that further reduces the contribution from reflections. The effective transform frequency  $f_{\text{eff}}$  is relatively small; thus, smoothed events in the fictitious time domain, such as refractions and guided events, give relatively large frequency-domain amplitudes compared with reflections even if their fictitious time-domain amplitudes are comparatively small. As stated in Appendix C, the effect of the inverse transform from the fictitious time domain to the diffusive frequency domain is that refractions and guided events are favored over reflected and diffracted events. At frequencies below 1 Hz, the reflections and diffractions are suppressed by the damping term and the

Figure 10. Damped normalized shot gather for the inline electric field. The frequency is 0.01 Hz.

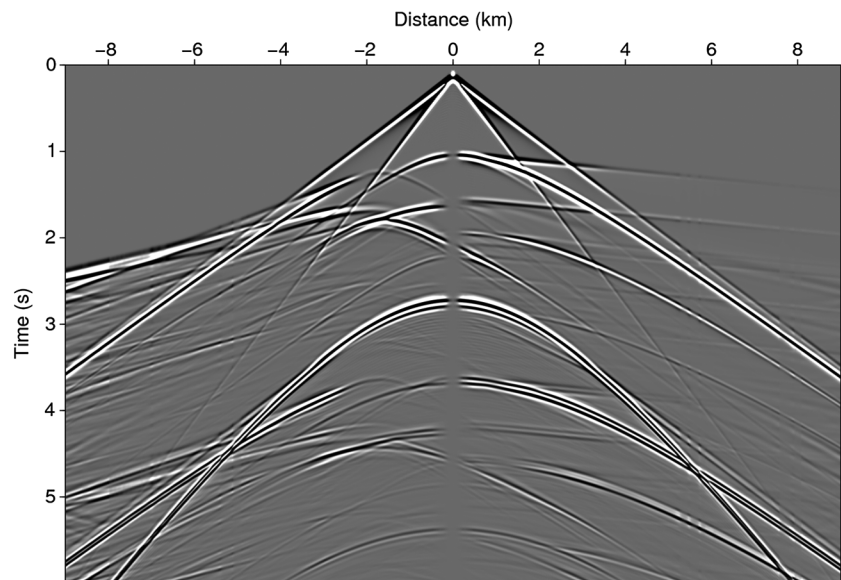
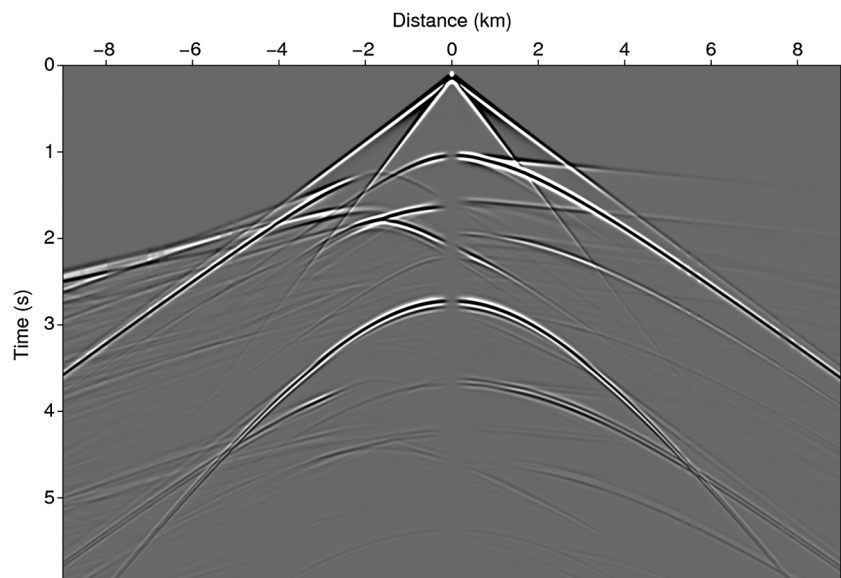


Figure 11. Damped normalized shot gather for the inline electric field. The frequency is 0.033 Hz.



phase term in the inverse transform. For higher frequencies, it is the damping term that suppresses reflections and diffractions relative to the earlier arriving refraction and guided events.

If the transmitter is elevated high above the seabed compared with the example given here, we may have a situation in which there are no refracted or guided events at small offsets. The only events are then the direct wave and precritical reflections. These types of events would then determine the marine CSEM response at small offsets. However, due to the large resistivity increase from the water to top formation and to a potential thin resistive layer, the critical angle for the onset of refracted events and guided events will be relatively small. The model shown in Figure 4 has a top formation resistivity of 1 ohm-m, and the critical angle is  $34^\circ$ . Suppose the transmitter is towed close to the sea surface and hence is 2.0 km above the seabed. The onset of refracted events in the seabed will then be at an offset of 1.35 km. For a top formation resistivity of

2 ohm-m, the critical angle will be  $23^\circ$  and the onset of refracted events in the seabed will then be at an offset of 860 m. It is clear that intermediate and large offsets, that is, offsets greater than 1.5 km, will be dominated by refracted and guided events also in the case of a surface towed transmitter even if the water depth is as large as 2.0 km. Thus, data recorded in a marine CSEM survey will behave similar to seismic refraction data.

The last observation is interesting when it comes to inversion of marine CSEM data. Full-waveform inversion (FWI) of marine CSEM data often shows remarkably good results, having the low-frequency content in mind. We can understand this by comparing the FWI of CSEM data with FWI of seismic data. Successful FWI of seismic data depends on having large offsets so that refraction type events are acquired. It is not uncommon to mute the later arriving reflections. Low-frequency data are important in seismic FWI because the cycle-skipping effect is small. Low-frequency data are

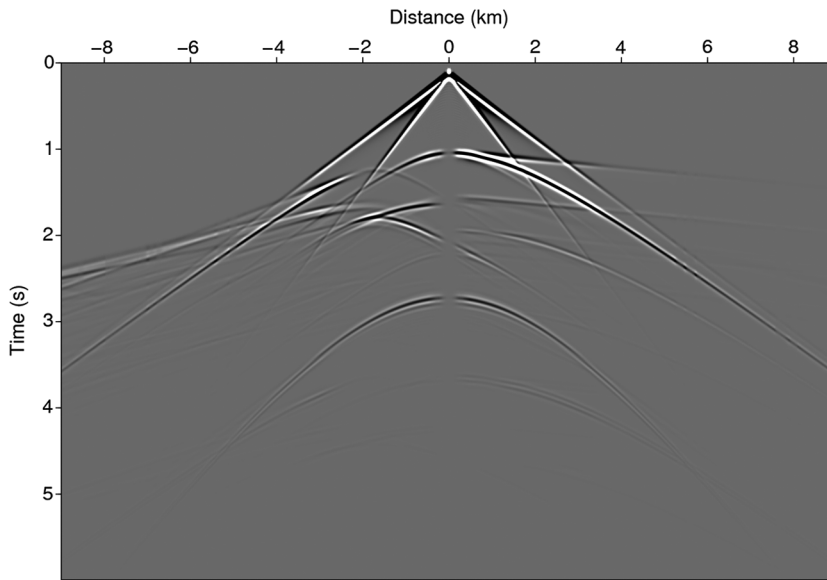


Figure 12. Damped normalized shot gather for the inline electric field. Frequency is 0.1 Hz.

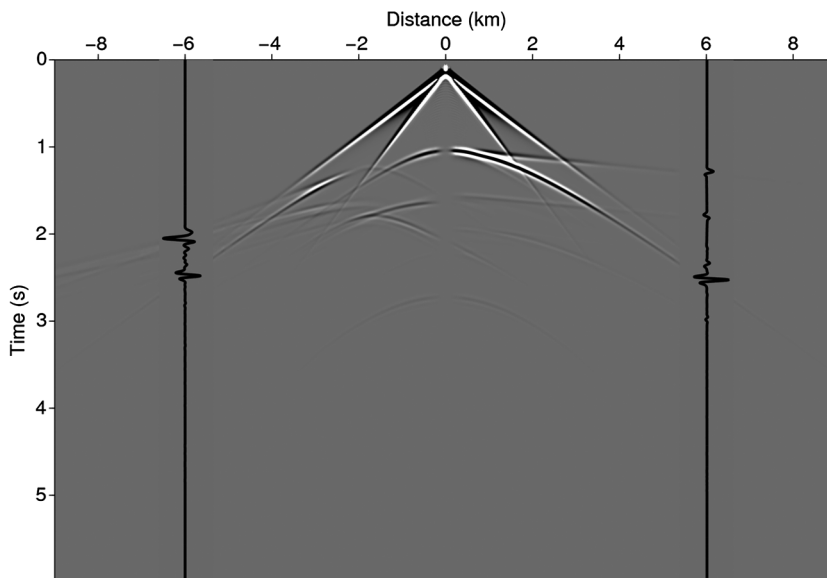


Figure 13. Damped normalized shot gather for the inline electric field. The frequency is 0.333 Hz. The traces at the  $-6$  km and  $+6$  km offsets are shown strongly amplified.

not always easy to obtain in the marine seismic case because airgun spectra are small for low frequencies. These properties are in place for marine CSEM data. Large source-receiver offsets are the standard. The skin depth effect due to the earth's conductivity forces us to transmit signals in the low-frequency range. In addition, the earth's conductivity properties favor refracted and guided events as the main contributions at intermediate and large offsets.

Interestingly, Virieux et al. (2012) propose to use a transform equivalent to equation 13 for seismic data to modify the objective function for FWI. The purpose is to mitigate the nonlinearity of the seismic inverse problem. The approach is related to, but not identical to, the Laplace transform technique proposed by Shin and Min (2006) as pointed out by Virieux et al. (2012). It is clear that equation 13 applied to seismic data will favor early arrivals over late arrivals due to the exponential damping term. This is a way to extract refractions and diving waves from the observed seismic data.

There is a second effect of the transform that may be beneficial for FWI of seismic data. It is already noted that seismic refracted events will experience a smoothing effect corresponding to an integration of the outgoing waveform. I have here shown that refractions can be enhanced relative to reflections and diffractions after the application of the transform in equation 13. This additional effect of the transform has effect also for transform frequencies that are so small that the damping effect for late arrivals is of less importance. The transform in equation 13 may be viewed as a filter for the seismic data that suppresses reflected and diffracted arrivals compared with refracted arrivals and diving waves.

Another question that comes naturally is whether diffusive electromagnetic (EM) data can be transformed to the fictitious time domain and processed with seismic processing software? As pointed out by de Hoop (1996), the operation of going from the wave domain to the diffusive domain is always stable. The reverse

Figure 14. Damped normalized shot gather for the inline electric field. The frequency is 1.0 Hz. The traces at the  $-6$  km and  $+6$  km offsets are shown strongly amplified.

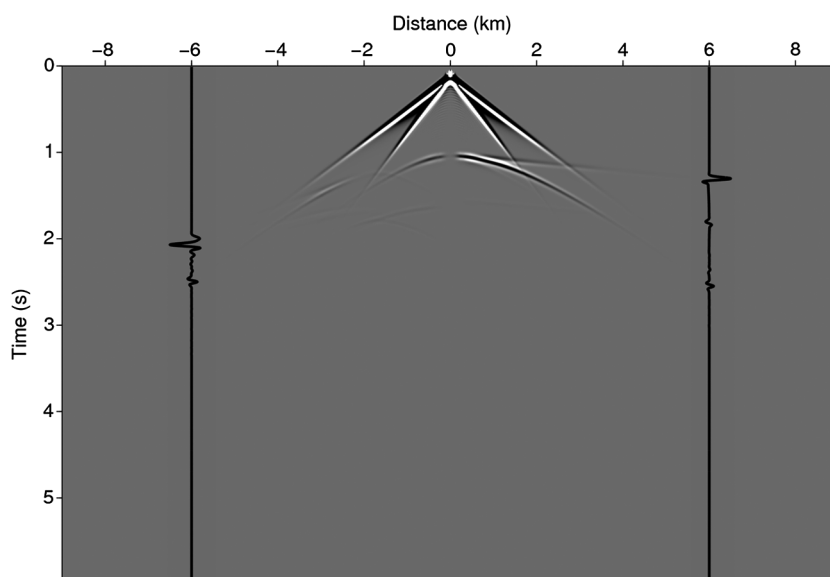
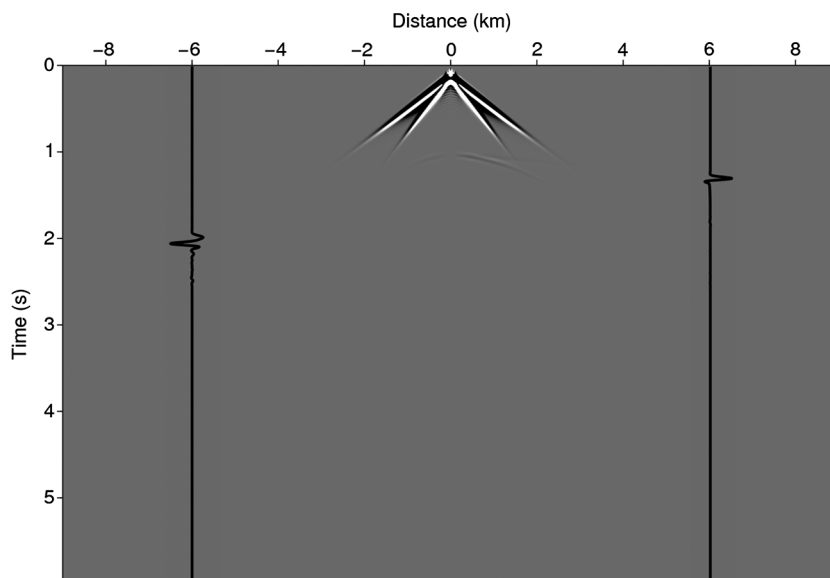


Figure 15. Damped normalized shot gather for the inline electric field. The frequency is 3.33 Hz. The traces at the  $-6$  km and  $+6$  km offsets are shown strongly amplified.



operation of going from the diffusive domain to the wave domain is an ill-posed problem. It can be done for a few frequencies at a time as discussed in [Mittet \(2010\)](#). This type of transform is necessary to calculate the adjoint state for gradient-based inverse schemes if a fictitious time-domain EM code is used for modeling. The problem of going from the diffusive domain to the wave domain for a wide frequency spectrum is still unsolved for noise-free synthetic data. Even if this part of the problem is solved, there is an additional issue with real data. The transform faces similar problems as  $Q$  compensation in seismic data processing. The noise will blow up as the

frequency is increased. The answer to the question posed above is negative as of today.

### Calibration

In Figure 16, I compare two different methods for the simulation of frequency-domain electric field responses from the resistivity model in Figure 4. The black curves show the inline electric field amplitude and phase. These solutions are obtained by applying the transform in equation 13 to the electric field data displayed in

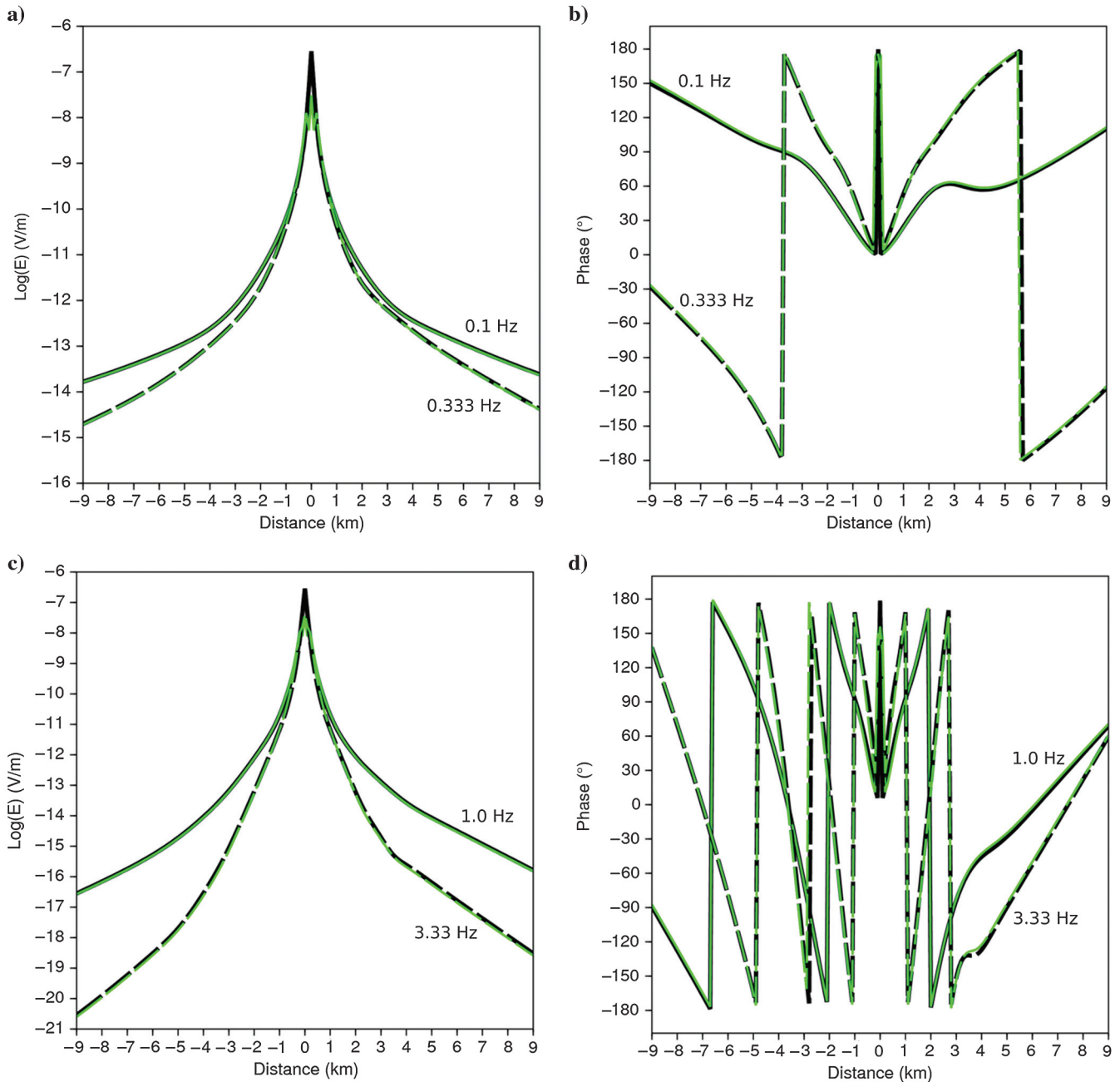


Figure 16. Amplitude and phase for the inline electric field. The black curves are for solutions using the fictitious wave-domain approach. The green curves are for solutions directly in the diffusive frequency domain. (a) Amplitudes versus offset for 0.1 Hz with solid lines and 0.333 Hz with dashed lines. (b) Phase versus offset for 0.1 Hz with solid lines and 0.333 Hz with dashed lines. (c) Amplitudes versus offset for 1.0 Hz with solid lines and 3.33 Hz with dashed lines. (d) Phase versus offset for 1.0 Hz with solid lines and 3.33 Hz with dashed lines.

Figure 7. The green curves also show the inline electric field amplitude and phase. These solutions are obtained by a direct frequency-domain solution of the diffusive field equation 7 as a linear equation system. No transform to or from the fictitious time domain is involved in this case. The solver used to generate the direct frequency-domain results is largely based on Mulder (2006), who uses a conjugate-gradient-type method in combination with a multigrid preconditioner and a block Gauss-Seidel smoother to solve the system of linear equations. The Gauss-Seidel smoother is required due to the large null-space of the curl-curl operator in 3D. The results in

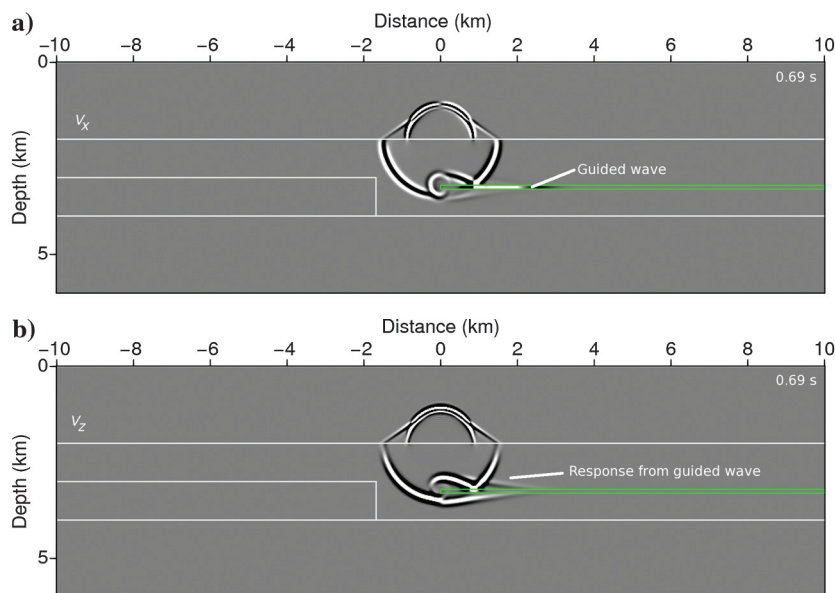


Figure 17. Snapshots of the  $x$ -component and  $z$ -component of the particle velocity for the variable density case.

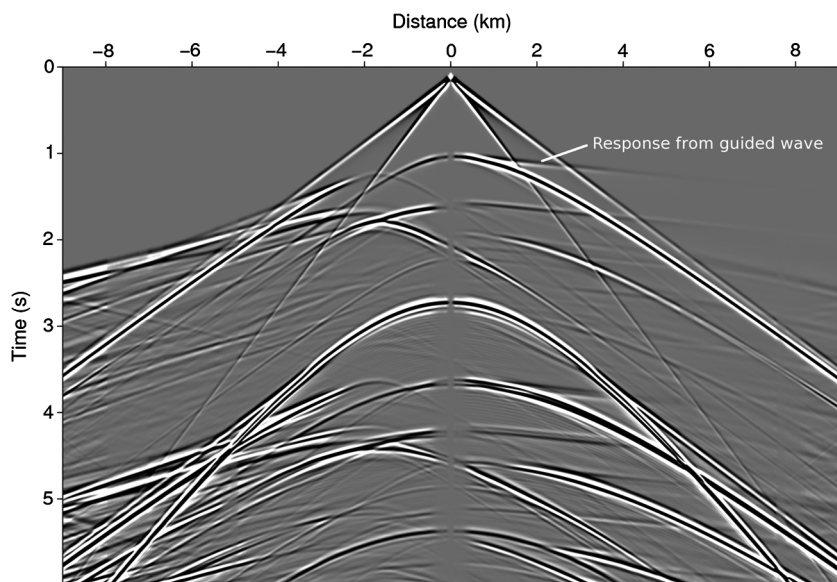


Figure 18. Normalized shot gather for the vertical component of particle velocity for the variable density case. The polarity is reversed.

Figure 16 are for frequencies from 0.1 up to 3.33 Hz. The resulting electric fields for the two simulation methods are close to identical over all offsets and all frequencies.

## CONCLUSIONS

The Maxwell equations in the quasistatic or diffusive limit can be transformed to a wave equation. The propagation of the fields can be analyzed in this transformed or fictitious time domain. Conclusions with regards to the real field propagation must take into account the properties of the inverse transform from the wave domain to the diffusive domain. There are two effects in the inverse transform that must be accounted for.

The first effect is that part of the inverse transform is an exponential damping of late arrivals. Thus, early arrivals in the wave domain are relatively more important than late arrivals. This effect becomes more pronounced with increased frequency. The recorded data in a marine CSEM survey configuration will be dominated by the first arrival if the frequency is sufficiently high. For a subsurface with a typical background resistivity of 1 ohm-m, this happens for frequencies above approximately 1.0 Hz. First arrivals in the wave domain are refractions if the resistivity increases with depth. First arrivals can also be guided events if thin resistive layers are present in the subsurface.

The second effect is more subtle and is related to the phase term in the inverse transform in combination with waveform modifications for refracted and guided events. Refracted and guided events are smoothed compared with reflected and diffracted events. The smoothing effect amounts to an amplification of the low frequency part of the spectra. The result is that refracted and guided events make relatively large contributions to the inverse transform from fictitious time to frequency when compared with reflections and diffractions. Thus, if refractions and reflections are present with equal amplitude along the same time trace, the inverse transform will give most weight to the refraction. This effect comes in addition to the damping of late arrivals, which normally are reflections and diffractions. The smoothing effect is most important for frequencies up to 1.0 Hz. Above 1.0 Hz, the inverse transform is dominated by the exponential damping term.

If the transmitter is close to the seabed, then refractions will dominate even at very small offsets. If the transmitter is surface-towed, there will be no refractions at small offsets and the CSEM data at these offsets will be dominated by the direct wave and the reflections. However, the resistivity contrast in the seabed is large, and the critical angle for the onset of refracted events is typically less than 35°. Consequently, even in the case of a surface-towed transmitter and a

2000-m water depth, we will have refractions as first arrivals for offsets above approximately 1500 m.

Concepts such as reflections, refractions, diffractions, and transmissions are valid for recorded events in a marine CSEM survey. Due to the earth properties, the transmitter properties, and the source/receiver configuration, we conclude that marine CSEM data are dominated by refracted and potentially guided events. Typical for marine CSEM data are significant field amplitudes for low frequencies only, large source-receiver offsets, and a high content of refraction events. These are attributes that are essential for the success of seismic FWI and may explain the relative success of FWI of marine CSEM data.

### ACKNOWLEDGMENTS

I would like to thank my colleague S. de la Kethulle de Ryhove for providing the simulation results from his direct frequency-domain solver for the Maxwell equations. I also thank J. Robertson, K. Wapenaar, and one anonymous reviewer for their fruitful suggestions and comments. Finally, I thank EMGS ASA for allowing the publication of this work.

### APPENDIX A

#### ACOUSTIC GUIDING

During the review process for this paper, one of the reviewers, K. Wapenaar, prompted me to take a closer look at acoustic guiding. In particular, he pointed to a paper by Wapenaar et al. (2001) in which a one-to-one correspondence between 2D EM wave equations and 2D acoustic wave equations is derived. We know that there is guiding effects for 2D EM waves in the transverse magnetic (TM) mode. As a consequence, there has to be compliance and density models that cause guiding effects in the 2D acoustics case. In particular, Table 1 of Wapenaar et al. (2001) shows that the compliance  $\kappa$  must be substituted for the magnetic permeability  $\mu$  when we transform from the 2D TM electromagnetic mode to the 2D acoustic mode. Likewise, the density  $\rho_{ac}$  must be substituted for the electric permittivity  $\epsilon$ , when we transform from the 2D TM electromagnetic mode to the 2D acoustic mode. This already gives us a hint that acoustic guiding in the form observed for the electromagnetic field is related to density variations in acoustics.

It turns out that the guiding effect is present also for 3D acoustics, but it will not happen for a constant density model as used in this paper up to now. Let us first have a closer look at EM guiding. The boundary conditions for the EM fields are obtained from the Maxwell equations. I assume a half-space model with a horizontal interface. The integral form of Ampère's law is by the application of Stokes' theorem:

$$\oint \mathbf{dl} \cdot \mathbf{H} = \partial_t \int \mathbf{dA} \cdot \mathbf{D} + \int \mathbf{dA} \cdot \mathbf{J}, \quad (\text{A-1})$$

where  $A$  is a surface area and  $\mathbf{dl}$  is a vector line element along the contour of  $A$ . Here,  $\mathbf{D} = \epsilon\mathbf{E}$  is the electric displacement. The surface area  $A$  is assumed to straddle the interface and be of length  $l_x$  or  $l_y$  and of height  $\Delta h$ . Taking the limit  $\Delta h \rightarrow 0$  under the assumption that there are no free charges in the system results in the two horizontal components of the magnetic field being continuous over the boundary. The assumption of no free charges is valid because the

Maxwell wave equation is for a dielectric medium, which do not permit any free charges. The integral form of Faraday's law is by the application of Stokes' theorem:

$$\oint \mathbf{dl} \cdot \mathbf{E} = -\partial_t \int \mathbf{dA} \cdot \mathbf{B}, \quad (\text{A-2})$$

where  $\mathbf{B} = \mu\mathbf{H}$  is the magnetic flux density. By similar reasoning as above, it can be deduced that the two horizontal components of the electric field are continuous over the boundary. These four boundary conditions are sufficient to determine the reflection and transmission properties of the electromagnetic field at the interface. However, the additional Maxwell equation,

$$\nabla \mathbf{D} = q, \quad (\text{A-3})$$

where  $q$  is the charge density, will determine the behavior of the vertical electric component at the boundary. The integral form of equation A-3 is by Gauss' theorem

$$\oint \mathbf{dA} \cdot \mathbf{D} = \int dV q = Q = 0, \quad (\text{A-4})$$

where  $V$  is the volume inside the closed surface  $A$  and  $Q$  is the total amount of free charge. The volume  $V$  also straddles the boundary and is  $V = l_x l_y \Delta h$ . In the limit of  $\Delta h \rightarrow 0$ , equation A-4 dictates that the vertical component of the electric displacement is continuous. Thus, if there is a jump in the electric permittivity, then there is a compensating jump in the vertical electric field:

$$E_z(2) = \frac{\epsilon(1)}{\epsilon(2)} E_z(1), \quad (\text{A-5})$$

where  $E_z(1)$  and  $\epsilon(1)$  are the values immediately above the interface and  $E_z(2)$  and  $\epsilon(2)$  are the values immediately below the interface. Equation 9, valid for the fictitious time-domain simulations, tells us that a jump in the "fictitious time domain" electric permittivity is proportional to a jump in the real-world conductivity. In particular, if the conductivity is greatly reduced in a thin layer, then the vertical electric field will compensate with a jump to a much higher value within the thin layer. This is also apparent from Figure 6b. The polarization is also favorable. The electromagnetic field in the inline direction propagates horizontally within the waveguide with a nearly transverse (vertical) polarization. This contains the essence of waveguide properties where the field is comparatively small outside the waveguide and acquires a large amplitude within the waveguide itself and where the polarization properties of the field within the waveguide are favorable.

The boundary conditions for the acoustic field can be obtained in a similar manner as above. The integral form of the constitutive relation is

$$\oint \mathbf{dA} \cdot \mathbf{v} = -\partial_t \int dV \kappa P. \quad (\text{A-6})$$

The resulting boundary condition is that the vertical component of the particle velocity  $v_z$  is continuous over the boundary under the assumption that the pressure  $P$  and the compliance  $\kappa$  are finite. Newton's second law, assuming that the boundary is at depth  $z_b$ , gives by integration in the  $z$ -direction

$$P(z_b + \Delta h/2) - P(z_b - \Delta h/2) = -\rho_{ac}(z_b)\partial_t v_z(z_b)\Delta h. \quad (\text{A-7})$$

Taking the limit  $\Delta h \rightarrow 0$  dictates the continuity of the pressure over the boundary. These two boundary conditions are sufficient to determine the reflection and transmission properties of the acoustic field at the interface in the acoustic case. However, we can also derive how the two horizontal components of the particle velocity behave over the boundary. Newton's second law can be written as

$$\partial_t \mathbf{p} = -\nabla P, \quad (\text{A-8})$$

where  $\mathbf{p} = \rho_{ac}\mathbf{v}$  is the particle momentum density of the field. Taking the curl of this equation results in

$$\partial_t \nabla \times \mathbf{p} = 0, \quad (\text{A-9})$$

which by Stokes' theorem results in

$$\oint \mathbf{dl} \cdot \mathbf{p} = 0. \quad (\text{A-10})$$

Thus, the two horizontal components of the particle momentum density must be continuous over the boundary. These two boundary conditions have similar effects as the continuity of the vertical electric displacement over the boundary. We observe that if the density makes a jump over the horizontal interface, then the horizontal particle velocities must also jump over the boundary to ensure continuity of the horizontal particle momentum densities:

$$v_x(2) = \frac{\rho_{ac}(1)}{\rho_{ac}(2)} v_x(1) \quad \text{and} \quad v_y(2) = \frac{\rho_{ac}(1)}{\rho_{ac}(2)} v_y(1). \quad (\text{A-11})$$

In particular, if the density is greatly reduced in a thin layer, then the horizontal particle velocities will compensate with jumps to much higher values within the thin layer. The polarization properties are favorable also in the acoustic case. The acoustic field propagates horizontally in the waveguide with longitudinal (horizontal) polarization. Again, this contains the essence of waveguide properties where the field is comparatively small outside the waveguide and acquires a large amplitude within the waveguide itself and where the polarization properties of the field within the waveguide are favorable.

For the acoustic model used in the main part of this paper, the density is kept constant and the velocity model variations are due to variations in compliance. The constant density approximation is a common assumption for the simulation and processing of seismic data because density variations in a sedimentary formation are believed to be relatively smaller than variations in elastic properties. In the case of constant density, the pressure and all three components of the particle velocity are continuous over the thin layer. This prevents a large jump for any of the field components, and the field polarization is not necessarily close to horizontal within the thin layer because the field polarization in this case is continuous and the polarization in the thin layer is locally the same as in the surrounding formation. An abrupt change of polarization for the acoustic field is closely linked to an abrupt change in density. For the electromagnetic field, the same type of amplitude gain and polarity rotation happens when the electric permittivity or the conductivity is reduced compared with the surrounding formation. The magnetic

permeability is close to that of the vacuum value except for ferromagnetic materials. It is common to use the vacuum value for sedimentary rock formations. In principle, a reduction in the magnetic permeability for a thin layer could cause waveguiding in a similar fashion as a reduction in electric permittivity. This would be a diamagnetic effect. However, diamagnetic effects are known to be weak, and such effects would never be observable in low-frequency geophysical applications.

The 3D acoustic model most similar to the 3D EM model used for the simulations in this paper is to keep the compliance constant and allow the density to vary in equation 2. The compliance is kept constant at the value for seawater. The density must then vary in such a way that the velocity model in Figure 1 is realized. The density in the thin layer becomes  $5.21 \text{ kg/m}^3$  compared with  $1000 \text{ kg/m}^3$  in the water layer. Such density variations are not geophysically realistic but can very well be studied in computer simulations.

Figure 17 shows snapshots at 0.69 s for the acoustic variable density simulation. The acoustic guiding effect is now present. There is an obvious similarity with the EM simulation results displayed in Figure 6. The polarity reversal on the  $v_z$  component compared with the  $E_x$  is in accordance with what Wapenaar et al. (2001) derive for 2D fields. For the example here, we have not performed a polarity reversal on the source function as required in Wapenaar et al. (2001). The result is that to compare with electromagnetic results, we have to do a polarity reversal on  $v_z$  instead of  $v_x$ . Figure 18 shows a normalized shot gather of  $v_z$  with the polarity reversed. This shot gather can be compared with the normalized shot gather for  $E_x$  in Figure 9. These shot gathers are in very good qualitative agreement, and the acoustic guiding is evident.

## APPENDIX B

### DE HOOP'S CORRESPONDENCE PRINCIPLE

The relations necessary for the discussion in this paper are derived in a rigorous manner by de Hoop (1996). The starting point for de Hoop is equations 5 and 8 as given in this paper. Equation 24 in de Hoop (1996) gives the transformation from the fictitious, wave time domain to the real, diffusive time domain. The description given by de Hoop is complete and valid for electric and magnetic fields with electric and magnetic sources. Here, I need the results for the electric field due to an electric dipole source. According to de Hoop (1996), the relation is

$$G_{ij}^{\text{EJ}}(\mathbf{x}, t|\mathbf{x}_s) = \left[ \int_0^\infty dt' W^{\text{EJ}}(t, t', \omega_0) G'_{ij}{}^{\text{EJ}}(\mathbf{x}, t'|\mathbf{x}_s) \right] H(t), \quad (\text{B-1})$$

where  $H(t)$  is the Heaviside step function. Compared with equation 24 in de Hoop (1996), the following changes in notation have been performed: The argument for fictitious time  $\tau$  in de Hoop (1996) is changed to  $t'$ , and the scale parameter  $\alpha$  in de Hoop (1996) is changed to  $2\omega_0$ . The Green's tensor in the fictitious time domain is here called  $G'_{ij}{}^{\text{EJ}}$ , and the Green's tensor for the real time domain is here called  $G_{ij}^{\text{EJ}}$ . The transform kernel  $W^{\text{EJ}}$  is defined by equations 26 and 29 in de Hoop (1996) and is



$$W^{EJ}(t, t', \omega_0) = -\frac{1}{2\omega_0} \partial_{t'} \left( \frac{1}{2} \sqrt{\frac{2\omega_0}{\pi}} \frac{t'}{t'^{3/2}} e^{-\frac{2\omega_0 t'^2}{4t'}} \right). \quad (\text{B-2})$$

A Fourier transform of equation B-1 gives the diffusive response in the frequency domain:

$$G_{ij}^{EJ}(\mathbf{x}, \omega | \mathbf{x}_s) = \int_{-\infty}^{\infty} dt G_{ij}^{EJ}(\mathbf{x}, t | \mathbf{x}_s) e^{i\omega t}, \quad (\text{B-3})$$

which is

$$G_{ij}^{EJ}(\mathbf{x}, \omega | \mathbf{x}_s) = \int_0^{\infty} dt \left[ \int_0^{\infty} dt' W^{EJ}(t, t', \omega_0) G_{ij}^{EJ}(\mathbf{x}, t' | \mathbf{x}_s) \right] e^{i\omega t}. \quad (\text{B-4})$$

I next add a small positive complex number to the frequency  $\omega \rightarrow \omega + i\epsilon$  with  $\epsilon$  positive and real and will later take the limit  $\epsilon \rightarrow 0^+$ . With  $s = \epsilon - i\omega$ , I obtain

$$G_{ij}^{EJ}(\mathbf{x}, \omega | \mathbf{x}_s) = -\frac{1}{2\omega_0} \int_0^{\infty} dt' G_{ij}^{EJ}(\mathbf{x}, t' | \mathbf{x}_s) [\partial_{t'} \mathcal{L}(t', \omega_0, s)], \quad (\text{B-5})$$

with

$$\mathcal{L}(t', \omega_0, s) = \int_0^{\infty} dt \left( \frac{1}{2} \sqrt{\frac{2\omega_0}{\pi}} \frac{t'}{t'^{3/2}} e^{-\frac{2\omega_0 t'^2}{4t'}} \right) e^{-st}. \quad (\text{B-6})$$

I introduce  $k = \sqrt{2\omega_0 t'}$  and obtain

$$\mathcal{L}(t', \omega_0, s) = \int_0^{\infty} dt \frac{1}{2} \frac{k}{\sqrt{\pi}} \frac{e^{-\frac{k^2}{4t'}}}{t'^{3/2}} e^{-st}. \quad (\text{B-7})$$

The integral is given as equation 29.3.82 in Abramowitz and Stegun (1970); thus,

$$\mathcal{L}(t', \omega_0, s) = e^{-k\sqrt{s}}. \quad (\text{B-8})$$

The above integral is convergent as  $\epsilon \rightarrow 0^+$  given that we choose the following roots:

$$\begin{aligned} \sqrt{s} &= \sqrt{\epsilon - i\omega} = p - iq, \\ p &= \sqrt{\frac{1}{2} \left( \sqrt{\epsilon^2 + \omega^2} + \epsilon \right)}, \\ \text{and} \\ q &= \sqrt{\frac{1}{2} \left( \sqrt{\epsilon^2 + \omega^2} - \epsilon \right)}, \end{aligned} \quad (\text{B-9})$$

which is  $\sqrt{s} = \sqrt{-i\omega} = (1-i)\sqrt{\omega/2}$ . The expression for  $\mathcal{L}$  can be written as

$$\mathcal{L}(t', \omega_0, s) = \mathcal{L}(t', \omega_0, \omega) = e^{-\sqrt{-2i\omega\omega_0}t'}. \quad (\text{B-10})$$

Equation B-5 now becomes

$$\begin{aligned} G_{ij}^{EJ}(\mathbf{x}, \omega | \mathbf{x}_s) &= -\frac{1}{2\omega_0} \int_0^{\infty} dt' G_{ij}^{EJ}(\mathbf{x}, t' | \mathbf{x}_s) \\ &\quad \times \left[ -\sqrt{-2i\omega\omega_0} e^{-\sqrt{-2i\omega\omega_0}t'} \right] \\ &= \sqrt{\frac{-i\omega}{2\omega_0}} \int_0^{\infty} dt' G_{ij}^{EJ}(\mathbf{x}, t' | \mathbf{x}_s) e^{-\sqrt{\omega\omega_0}t'} e^{i\sqrt{\omega\omega_0}t'}. \end{aligned} \quad (\text{B-11})$$

The relation between equations B-11 and 13 is as follows: Suppose the fictitious time-domain field in equation 13 is excited with temporal and spatial Dirac distributions with source current direction in the  $j$ -direction. It would then be appropriate to write equation 13 as

$$E_{ij}(\mathbf{x}, \omega | \mathbf{x}_s) = \int_0^T dt' G_{ij}^{EJ}(\mathbf{x}, t' | \mathbf{x}_s) e^{-\sqrt{\omega\omega_0}t'} e^{i\sqrt{\omega\omega_0}t'}. \quad (\text{B-12})$$

Equation 20 of Mittet (2010) can be written as

$$G_{ij}^{EJ}(\mathbf{x}, \omega | \mathbf{x}_s) = \frac{E_{ij}(\mathbf{x}, \omega | \mathbf{x}_s)}{J^T(\omega)}, \quad (\text{B-13})$$

with

$$J^T(\omega) = \sqrt{\frac{-2\omega_0}{i\omega}} \int_0^T dt' J^{iT}(t') e^{-\sqrt{\omega\omega_0}t'} e^{i\sqrt{\omega\omega_0}t'}. \quad (\text{B-14})$$

For  $J^{iT}(t') = \delta(t' - 0^+)$ ,

$$J^T(\omega) = \sqrt{\frac{-2\omega_0}{i\omega}}, \quad (\text{B-15})$$

and equations B-12, B-13, and B-15 give

$$G_{ij}^{EJ}(\mathbf{x}, \omega | \mathbf{x}_s) = \sqrt{\frac{-i\omega}{2\omega_0}} \int_0^T dt' G_{ij}^{EJ}(\mathbf{x}, t' | \mathbf{x}_s) e^{-\sqrt{\omega\omega_0}t'} e^{i\sqrt{\omega\omega_0}t'}, \quad (\text{B-16})$$

which is identical to the result in equation B-11 and validates the use of equation 13 in the discussions in this paper.

## APPENDIX C

### ON TIME AND FREQUENCY TRANSFORMATIONS

There are two frequencies referred to in the discussions in this paper. This may cause some confusion. Let  $E'_i(\mathbf{x}, t')$  be an electric field component in the fictitious time domain. This field can be decomposed into its Fourier components  $E'_i(\mathbf{x}, \omega')$ :

$$E'_i(\mathbf{x}, \omega') = \int_0^T dt' E'_i(\mathbf{x}, t') e^{i\omega' t'}, \quad (\text{C-1})$$

where the angular frequency  $\omega'$  is real. The inverse transform, assuming an angular Nyquist frequency  $\omega_N$ , is

$$E_i'(\mathbf{x}, t') = \frac{1}{2\pi} \int_{-\omega_N}^{\omega_N} d\omega' E_i'(\mathbf{x}, \omega') e^{-i\omega' t'}. \quad (\text{C-2})$$

These two equations are used when the frequency content of the fictitious time-domain signal is discussed.

On the other hand, the diffusive frequency-domain response is

$$E_i(\mathbf{x}, \omega) = \int_0^T dt' E_i'(\mathbf{x}, t') e^{i\omega_c t'}, \quad (\text{C-3})$$

where  $\omega_c = (1+i)\sqrt{\omega\omega_0} = (1+i)\omega_{\text{eff}}$ .

The relation between peak amplitude in the fictitious time domain and the absolute value of the complex amplitude in the diffusive frequency domain can be explained by using Gaussian waveforms. This is relevant because these are the types of waveforms occurring in the electromagnetic wave simulations. Let  $\Gamma(t')$  be a Gaussian. The first-order derivative with respect to time is  $\dot{\Gamma}(t') = \partial_{t'}\Gamma(t')$ , and the second-order derivative with respect to time is  $\ddot{\Gamma}(t') = \partial_{t'}^2\Gamma(t')$ . The peak values of the waveforms are at  $t' = t'_{\text{peak}}$ . For the Gaussian, we have

$$\begin{aligned} \Gamma(t') &= \sqrt{\frac{\beta}{\pi}} e^{-\beta(t'-t_0)^2}, \\ t'_{\text{peak}} &= t_0, \\ \text{and} \\ |\Gamma(t'_{\text{peak}})| &= \sqrt{\frac{\beta}{\pi}}. \end{aligned} \quad (\text{C-4})$$

For the first-order derivative of the Gaussian, we have

$$\begin{aligned} \dot{\Gamma}(t') &= -\sqrt{\frac{\beta}{\pi}} 2\beta(t'-t_0) e^{-\beta(t'-t_0)^2}, \\ t'_{\text{peak}} &= t_0 \pm \frac{1}{\sqrt{2\beta}}, \\ \text{and} \\ |\dot{\Gamma}(t'_{\text{peak}})| &= \sqrt{\frac{\beta}{\pi}} \sqrt{2\beta} e^{-\frac{1}{2}}. \end{aligned} \quad (\text{C-5})$$

For the second-order derivative of the Gaussian, we have

$$\begin{aligned} \ddot{\Gamma}(t') &= -\sqrt{\frac{\beta}{\pi}} 2\beta[1 - 2\beta(t'-t_0)^2] e^{-\beta(t'-t_0)^2}, \\ t'_{\text{peak}} &= t_0, \\ \text{and} \\ |\ddot{\Gamma}(t'_{\text{peak}})| &= \sqrt{\frac{\beta}{\pi}} 2\beta. \end{aligned} \quad (\text{C-6})$$

The transform from fictitious time to diffusive frequency gives

$$\begin{aligned} \Gamma(\omega) &= \int_0^T dt' \Gamma(t') e^{-\sqrt{\omega\omega_0} t'} e^{i\sqrt{\omega\omega_0} t'} \\ &= e^{-\sqrt{\omega\omega_0} t_0} e^{i\sqrt{\omega\omega_0} t_0} e^{-i\frac{\omega\omega_0}{2\beta}}, \\ |\Gamma(\omega)| &= e^{-\sqrt{\omega\omega_0} t_0}, \end{aligned} \quad (\text{C-7})$$

$$\begin{aligned} \dot{\Gamma}(\omega) &= \int_0^T dt' \dot{\Gamma}(t') e^{-\sqrt{\omega\omega_0} t'} e^{i\sqrt{\omega\omega_0} t'} \\ &= (1-i)\sqrt{\omega\omega_0} e^{-\sqrt{\omega\omega_0} t_0} e^{i\sqrt{\omega\omega_0} t_0} e^{-i\frac{\omega\omega_0}{2\beta}}, \\ |\dot{\Gamma}(\omega)| &= \sqrt{2\omega\omega_0} e^{-\sqrt{\omega\omega_0} t_0}, \end{aligned} \quad (\text{C-8})$$

and

$$\begin{aligned} \ddot{\Gamma}(\omega) &= \int_0^T dt' \ddot{\Gamma}(t') e^{-\sqrt{\omega\omega_0} t'} e^{i\sqrt{\omega\omega_0} t'} \\ &= -2i\omega\omega_0 e^{-\sqrt{\omega\omega_0} t_0} e^{i\sqrt{\omega\omega_0} t_0} e^{-i\frac{\omega\omega_0}{2\beta}}, \\ |\ddot{\Gamma}(\omega)| &= 2\omega\omega_0 e^{-\sqrt{\omega\omega_0} t_0}. \end{aligned} \quad (\text{C-9})$$

For the time domain, we can compare the peak amplitude of the second-order derivative of the Gaussian to the peak amplitude of the first-order derivative of the Gaussian:

$$R_T = \frac{|\ddot{\Gamma}(t'_{\text{peak}})|}{|\dot{\Gamma}(t'_{\text{peak}})|} = \sqrt{2\beta} e. \quad (\text{C-10})$$

For the frequency domain, we can compare the absolute value of the complex amplitude of the second-order derivative of the Gaussian to the absolute value of the complex amplitude of the first-order derivative of the Gaussian:

$$R_\Omega(\omega) = \frac{|\ddot{\Gamma}(\omega)|}{|\dot{\Gamma}(\omega)|} = \sqrt{2\omega\omega_0}. \quad (\text{C-11})$$

In the simulations performed for this paper, I have used  $\beta = 1640$ , which gives a maximum frequency of approximately 23 Hz (see [Mittet, 2010](#)). Assuming that there are no additional scale factors for the time-domain functions, I find that the peak amplitude of the second-order derivative of the Gaussian is 95 times larger than the peak amplitude of the first-order derivative of the Gaussian. The value for the scale parameter is  $\omega_0 = 2\pi f_0$  with  $f_0 = 0.7198$  Hz. For a frequency of  $f = 0.333$  Hz, I find, using equation C-11, that the absolute value of the complex amplitude of the second-order derivative of the Gaussian is only four times larger than the complex amplitude of the first-order derivative of the Gaussian. Thus, a waveform proportional to the first-order derivative of a Gaussian can be a factor of 23 smaller than a waveform proportional to the second-order derivative of a Gaussian and still give a comparable contribution after the transform from the fictitious wave domain to the diffusive frequency domain. If the transform frequency is  $f = 0.033$  Hz, then the absolute value of the complex amplitude of the second-order derivative of the Gaussian is 1.35 times larger than the complex amplitude of the first-order derivative of the Gaussian; in this case, a waveform proportional to the first-order

derivative of a Gaussian can be a factor of 70 smaller than a wave-form proportional to the second-order derivative of a Gaussian and still give the same contribution after the transform from the fictitious wave domain to the diffusive frequency domain. The effect of the inverse transform from the fictitious time domain to the diffusive frequency is that refractions and guided events are favored over reflected and diffracted events. At frequencies below 1 Hz, the reflections and diffractions are suppressed by the damping term and the phase term in the inverse transform. For higher frequencies, it is the damping term that suppresses reflections and diffractions relative to the earlier arriving refractions and guided events.

## REFERENCES

- Abramowitz, M., and I. A. Stegun, 1970, *Handbook of mathematical functions*: Dover Publications, Inc.
- Aki, K., and P. G. Richards, 1980, *Quantitative seismology*: W.H. Freeman and Co.
- Amundsen, L., and R. Mittet, 1994, Estimation of phase velocities and  $Q$ -factors from zero offset vertical seismic profile data: *Geophysics*, **59**, 500–517, doi: [10.1190/1.1443612](https://doi.org/10.1190/1.1443612).
- Auld, B. A., 1973, *Acoustic fields and waves in solids*: John Wiley and Sons, Inc.
- Carcione, J. M., 2007, *Wave fields in real media: Wave propagation in anisotropic, anelastic, porous and electromagnetic media*: Elsevier, *Handbook of Geophysical Exploration: Seismic Exploration*, vol. 38.
- de Hoop, A. T., 1996, A general correspondence principle for time-domain electromagnetic wave and diffusion fields: *Geophysical Journal International*, **127**, 757–761, doi: [10.1111/j.1365-246X.1996.tb04054.x](https://doi.org/10.1111/j.1365-246X.1996.tb04054.x).
- Lee, K. H., G. Liu, and H. F. Morrison, 1989, A new approach to modeling the electromagnetic response of conductive media: *Geophysics*, **54**, 1180–1192, doi: [10.1190/1.1442753](https://doi.org/10.1190/1.1442753).
- Løseth, L. O., and B. Ursin, 2007, Electromagnetic fields in planarly layered anisotropic media: *Geophysical Journal International*, **170**, 44–80, doi: [10.1111/j.1365-246X.2007.03390.x](https://doi.org/10.1111/j.1365-246X.2007.03390.x).
- Mittet, R., 2010, High-order finite-difference simulations of marine CSEM surveys using a correspondence principle for wave and diffusion fields: *Geophysics*, **75**, no. 1, F33–F50, doi: [10.1190/1.3278525](https://doi.org/10.1190/1.3278525).
- Mittet, R., O. Holberg, B. Amtsen, and L. Amundsen, 1988, Fast finite-difference modeling of 3D elastic wave propagation: 58th Annual International Meeting, SEG, Expanded Abstracts, 1308–1311.
- Mittet, R., and J. P. Morten, 2013, The marine controlled-source electromagnetic method in shallow water: *Geophysics*, **78**, no. 2, E67–E77, doi: [10.1190/geo2012-0112.1](https://doi.org/10.1190/geo2012-0112.1).
- Mulder, W. A., 2006, A multigrid solver for 3D electromagnetic diffusion: *Geophysical Prospecting*, **54**, 633–649, doi: [10.1111/j.1365-2478.2006.00558.x](https://doi.org/10.1111/j.1365-2478.2006.00558.x).
- Newman, P. J., and M. H. Worthington, 1982, In-situ investigation of seismic body wave attenuation in heterogeneous media: *Geophysical Prospecting*, **30**, 377–400, doi: [10.1111/j.1365-2478.1982.tb01312.x](https://doi.org/10.1111/j.1365-2478.1982.tb01312.x).
- Shin, C., and D. Min, 2006, Waveform inversion using a logarithmic wavefield: *Geophysics*, **71**, no. 3, R31–R42, doi: [10.1190/1.2194523](https://doi.org/10.1190/1.2194523).
- Ursin, B., 1983, Review of elastic and electromagnetic wave propagation in layered media: *Geophysics*, **48**, 1063–1081, doi: [10.1190/1.1441529](https://doi.org/10.1190/1.1441529).
- Ursin, B., and A. Stovas, 2002, Reflection and transmission responses of a layered isotropic viscoelastic medium: *Geophysics*, **67**, 307–323, doi: [10.1190/1.1451803](https://doi.org/10.1190/1.1451803).
- Virieux, J. M., R. Brossier, S. Garambois, S. Operto, and A. Ribodetti, 2012, Making seismic data as CSEM data through the Bäcklund transform: Presented at 5th Saint Petersburg International Conference and Exhibition.
- Wapenaar, C. P. A., M. W. P. Dillen, and J. T. Fokkema, 2001, Reciprocity theorems for electromagnetic or acoustic one-way wave fields in dissipative inhomogeneous media: *Radio Science*, **36**, 851–863, doi: [10.1029/2000RS002394](https://doi.org/10.1029/2000RS002394).
- White, J. E., 1965, *Seismic waves: Radiation, transmission, and attenuation*: McGraw-Hill.